UNIVERSITA' DEGLI STUDI DI MILANO

Dipartimento di Scienze Biomediche per la Salute

PhD course in

Integrative Biomedical Research (R23)

XXXIII Cycle

Identification of a novel sinoatrial node activity regulator: the proteohormone FGF23

Tutor: Prof. Mirko Baruscotti

Co-Tutor: Prof.ssa Annalisa Bucchi

Coordinator: Prof.ssa Chiarella Sforza

Dott.ssa Giorgia Bertoli

Matr. R12110

Academic Year 2019-2020

Index

PREFACE ..... - 5 -

INTRODUCTION ..... - 6 -
Electrical activity of the heart ..... - 6 -
The conduction system of the heart ..... - 6 -
Action Potential ..... - 7 -
SAN Automaticity Intrinsic control ..... - 9 -
The funny current ..... - 9 -
HCN channels ..... - 10 -
The L-Type and T-Type calcium currents ..... - 11 -
Voltage gated calcium channels ..... - 12 -
Calcium Clock ..... - 13 -
SAN Automaticity extrinsic control ..... - 14 -
Autonomic control of heart rate ..... - 14 -
Hormonal control of the heart rate ..... - 15 -
FGF family ..... - 16 -
FGFR ..... - 17 -
α-KLOTHO ..... - 18 -
FGF23 ..... - 19 -
FGF23 Renal Action ..... - 19 -
FGF23 Regulation of Production ..... - 20 -
FGF23 and α-Klotho KO mouse models ..... - 21 -
FGF23 and α-Klotho disorders in human ..... - 22 -
FGF23-different activation pathway ..... - 23 -
FGF23 Heart action ..... - 24 -
α-Klotho cardioprotective role ..... - 25 -

AIM ..... - 26 -

RESULTS ..... - 27 -
Mouse Sinoatrial node analysis ..... - 27 -
Human Induced Pluripotent Stem cells (hIPSC) derived- 38 -cardiomyocytes analysis ..... - 38 -

DISCUSSION ..... - 42 -

MATERIALS AND METHODS ..... - 46 -
Animals ..... - 46 -
Mouse SAN cells isolation ..... - 46 -
SAN tissue incubation ..... - 47 -
Human induced pluripotent stem cells-derived cardiomyocytes ..... - 47 -
Functional studies in mouse SAN cells ..... - 48 -
Functional studies (hiPSC) derived cardiomyocytes ..... - 50 -
Reverse transcriptase PCR (RT-PCR) analysis ..... - 51 -
Reverse transcriptase (RT) quantitative PCR (qPCR) analysis ..... - 51 -
Immunofluorescence analysis ..... - 52 -
Western blotting analysis ..... - 53 -
Primary Antibodies ..... - 54 -
Statistical Analysis ..... - 54 -

SUPPLEMENTARY MATERIALS ..... - 55 -

BIBLIOGRAPHY ..... - 56 -

Preface

FGF23 is a proteohormone mainly produced by osteocytes and osteoblasts whose canonical effect is to regulate the mineral metabolism through the FRS2 α/MAPK pathway activation[1]. This hormone exerts its function mostly in the kidneys where it binds the FGF Receptor (FGFR) complex, which is composed by the FGFR and the specific FGF23 co-receptor, α- Klotho[2].

Although the heart is not considered a canonical FGF23 target, data from Takeshita and colleagues[3] highlight the expression of α-Klotho in the Sino-Atrial Node (SAN), the natural pacemaker of the heart and, interestingly, α-Klotho KO mice display intrinsic bradycardia and easily perish for sinus arrest or sinus block as a consequence of restrain stress. This suggests that SAN cells, as well as tubular renal cells, might be a physiological FGF23 target.

Real-time and immunofluorescence experiments reveal that mouse SAN cells express both membrane α-Klotho and FGFRs (mainly FGFR1), and patch-clamp experiments have shown that incubating the SAN with FGF23 for 48hrs increases the spontaneous AP frequency of these cells through an increase in the I_f current conductance without affecting channel voltage dependence. Similar patch clamp experiments carried out using the pan-FGFR inhibitor, PD173074, and SAN cells isolated from α-Klotho KO mice suggested that FGF23 effects are mediated by the activation of the FGFR1-α-Klotho complex which can ultimately increase f-channels synthesis or decrease channel degradation. Our data also suggest that ERK phosphorylation might be part of the pathway linking the receptor complex activation to I_f increase. The data obtained in the mouse model were further confirmed in hiPSC-derived spontaneously beating cardiomyocytes; indeed, patch-clamp experiments reveal that the incubation with FGF23 1ng/mL for 48hrs increases both the AP frequency and the I_f current density. Since we were able to observe the same results in the two different pacemaker models (mice SAN and hiPSC-derived spontaneously beating cardiomyocytes) we can speculate that our findings might be applicable also to a human SAN.

In conclusion this study demonstrates for the first time that FGF23 can regulate SAN electrical activity and provides novel insights into the cardio-renal axis.

Introduction

Electrical activity of the heart

The heart is composed by two populations of myocytes: the working myocardium, which is mainly involved in cardiac contractility, and the conduction system, which is specialized in the generation and transmission of the cardiac electrical impulse.

The conduction system of the heart

The cardiac conduction system consists of the Sino Atrial Node (SAN), also called sinus node, the atrioventricular (AV) node and the His–Purkinje system (Figure 1).
The SAN is the natural pacemaker of the heart; it is located in the right atrium and its able to generate the electrical impulse, the action potential (AP), which is spread to adjacent atrial myocardial cells through the gap junctions and via the conduction system in the whole organ.
The AV node is part of the AV conduction axis that connects the atria to the ventricles, it slows the electrical impulse to allow the beginning of the ventricular systole only at the end of the atrial systole. The AV node also shows pacemaker potentiality, but its rate is slower than the SAN. Only when the SAN is not able to fulfill its role, the AV node can take over and become the main pacemaker.

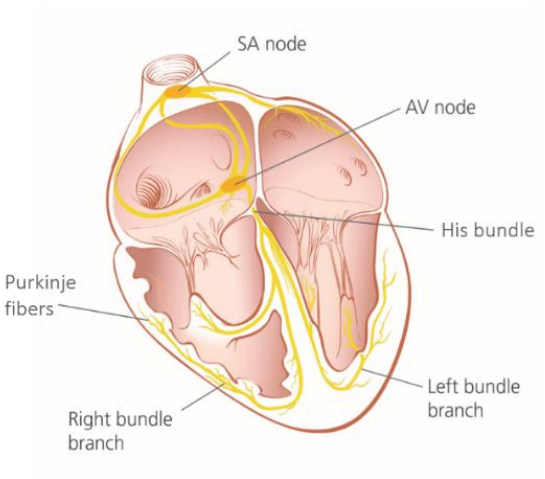

Figure 1. The conduction system of the heart. The specialized conduction system is constituted by the Sino Atrial (SA) node, the Atrio Ventricular (AV) node and the bundle of His, that splits into the right and left branches and ended with Purkinje fibres.

The portion of the cardiac conduction system that goes from the AV node to the ventricles is formed by the His bundle which terminates with the Purkinje network. The structure of these system

ensures the synchronous activation and contraction of the ventricular myocardium to achieve the most efficient pumping activity of the organ.

Action Potential

The AP consists in a rapid voltage alteration across the membrane of the cell; it is due to a sequence of ion fluxes through specialized channels located in the cardiomyocyte's membrane. Distinct heart regions show different AP waves owing to differences in the expression and the properties of the ion channels. In Figure 2 distinct regions of the heart that show different spontaneous AP waves are illustrated.

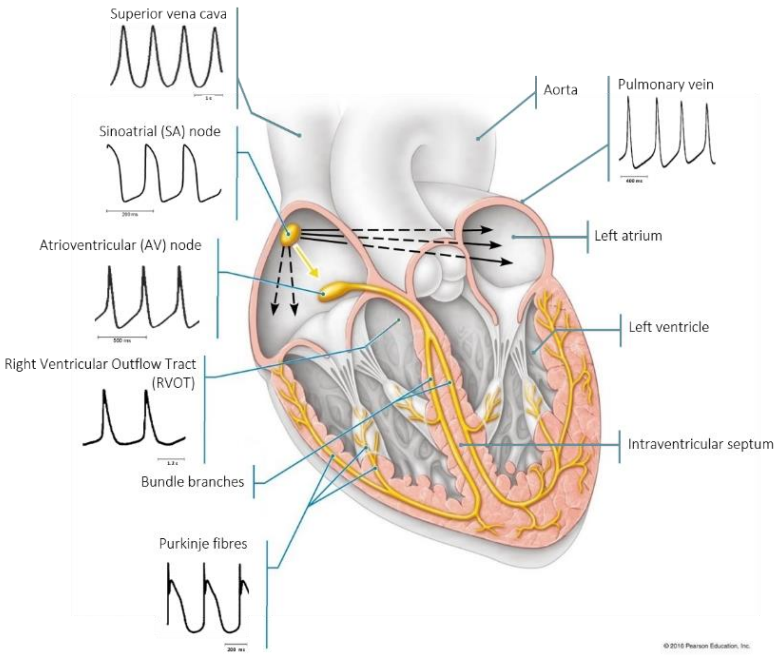

Figure 2. Variety of heart spontaneous AP. Representation of human heart with illustration of typical spontaneous AP recorded from the superior vena cava (dog, 37°C[4]), the SAN (rabbit, 35°C; D. Molla, unpublished data), the AVN (rabbit, 35–37°C[5]), the RVOT (rabbit, 37°C; S.J.R.J. Logantha, unpublished data), Purkinje fibers (rabbit, free running; 37°C; S.J.R.J. Logantha, unpublished data) and pulmonary veins (rabbit, 37°C[6]). All records were acquired in tissue preparations with the exception of SAN, AVN and superior vena cava recordings, which were obtained from isolated myocytes (modified from Dobrzynski et al., 2013[7]).

In brief, we can divide the APs in two major groups: the spontaneous AP typical of the SAN and the AV node and the induced AP typical of atrial and ventricular myocardium (Figure 3).
During diastole the membrane potential of a ventricular cell is maintained at the resting value of about -90 mV by the presence of the inward rectifier current (I_{k1}) until a new depolarizing stimulus arrives (phase 4).

In the SAN cells the phase 4 is also named slow diastolic depolarization (SDD); indeed this cells do not present a resting state, they reach their maximum diastolic potential, MDP (about -60 mV), stay at this potential only for a small fraction of time and slowly depolarize. The SDD is sustained by two processes: the "membrane or voltage-clock," resulting from a flow of ions through the membrane channels, and the "calcium-clock," resulting from the intracellular calcium cycling. The first part of this AP phase is established by the inactivation of the outward potassium currents (I_{Kr}, I_{Ks})[8] and the activation of the inward I_f current[9]; the last part of the SDD is manly sustained by the L-type calcium $Ca_v1.3$ channels and slightly by T-type Calcium $Ca_v3.1$ channels[10]. Furthermore, in the last part of the SDD the calcium-clock plays its role; indeed, the sarcoplasmic reticulum (SR), via ryanodine receptors (RyRs), releases spontaneous, or $Ca_v1.3$ channels-triggered, Ca^{2+} ions in the cytoplasm. The Ca^{2+}-Na^+ exchanger (NCX), situated on the plasmatic membrane, in turn extrudes 1 Ca^{2+} ion for 3 Na^+ ions resulting in a depolarizing current generation[11,12].

L-type Calcium $Ca_v1.2$ channels instead seem to be more important in generating the upstroke phase of the AP (phase 0)[13].

On the other hand, non-pacemaker cells remain at -90 mV until an external stimulus brings the voltage over the threshold (about -70 mV) for the activation of the voltage-gated Na^+ (Na_v) channels which induce a large and rapid inward sodium inflow (fast membrane depolarization or phase 0). After the upstroke the AP undergoes three distinctive phases:

- Phase 1: a partial repolarization caused by the opening of transient outward K^+ channels (I_{to});
- Phase 2: the plateau phase, sustained by the balance of an inward calcium current generated by L-type calcium channels and outward potassium currents (I_{Kr}, I_{Ks}). It allows the maintenance of the membrane potential near 0 mV for about 200 ms; in this phase Ca^{2+} influx through the L-type calcium channels triggers Ca^{2+} release from intracellular stores causing the excitation-contraction coupling;
- Phase 3: the repolarization to the resting value is due to the inactivation of L-type calcium channels and the active presence of I_{Kr} and I_{Ks} repolarizing currents.

Otherwise, after the upstroke, SAN cells immediately present a phase 3 of hyperpolarization since K^+ channels open and the L-type Ca^{2+} channels become inactivated.

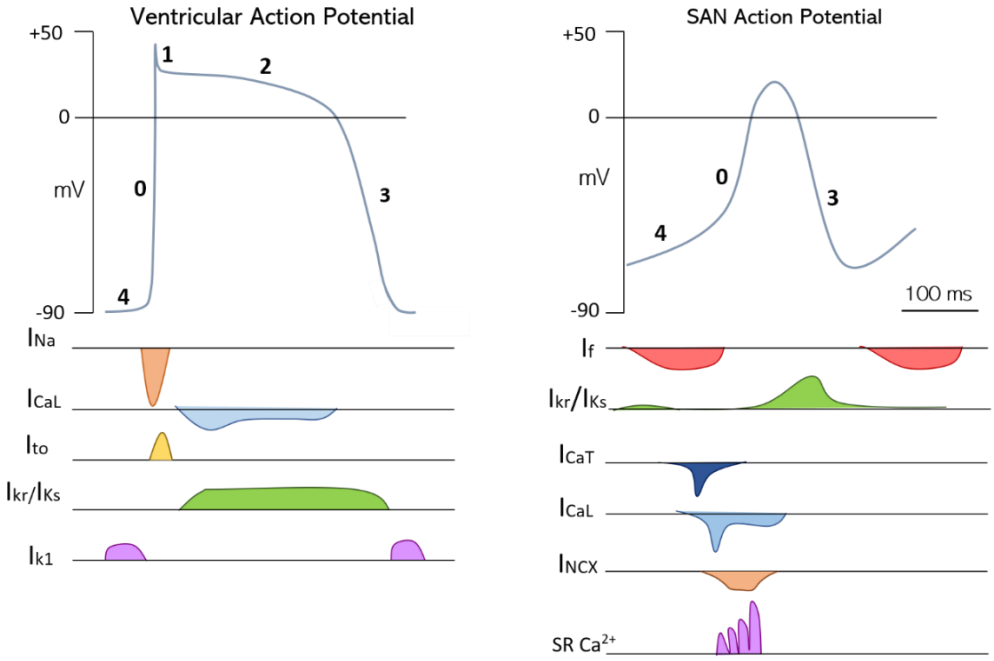

Figure 3. Ventricular and SAN APs. Illustration of ventricular and SAN APs waveforms highlighting the currents accountable for the different AP phases.

SAN Automaticity Intrinsic control

The SAN is the natural pacemaker of the heart, thus it establishes the intrinsic heart rate; because SAN activity it is so crucial, many redundant systems are involved in maintaining its function. Therefore, I_f, I_{CaL} and I_{CaT} currents, that together have been delineated as ion channel membrane clock, work in concert with the calcium clock to preserve the SAN automaticity in a mechanism defined coupled clock[14].

The principal mechanisms implicated in the SDD of SAN APs are discussed in the following paragraphs.

The funny current

The funny (I_f) current, also called pacemaker current, is responsible for initiating the diastolic depolarization of SAN cells conferring them spontaneous automaticity. Due to its unusual characteristics, this current was named "funny"[9]. As well as being activated by hyperpolarization (at about -40/-45 mV), it presents other uncommon characteristics:

- a mixed sodium and potassium conduction, with a resulting reversal potential of about -10/-20 mV[15].
- cyclic AMP (cAMP) regulation: cAMP increases the open probability of pacemaker channels by a direct binding[16].

The cytosolic concentration of the second messenger cAMP is regulated by the autonomic nervous system. Briefly, the parasympathetic agonist acetylcholine, activating muscarinic M2 receptors, inhibits adenylate cyclase decreasing intracellular cAMP concentration; on the contrary, the sympathetic neurotransmitter noradrenaline, triggering β-adrenergic (β1 and β2) receptors, increases the intracellular cAMP concentration.

In SAN cells the increase/decrease of intracellular cAMP shifts the I_f activation curve to more positive/negative voltages. This causes an increase/decrease of the net inward I_f current causing an increment/reduction of the steepness of the diastolic depolarization phase and a consequent increase/decrease of firing rate, respectively (Figure 4)[17].

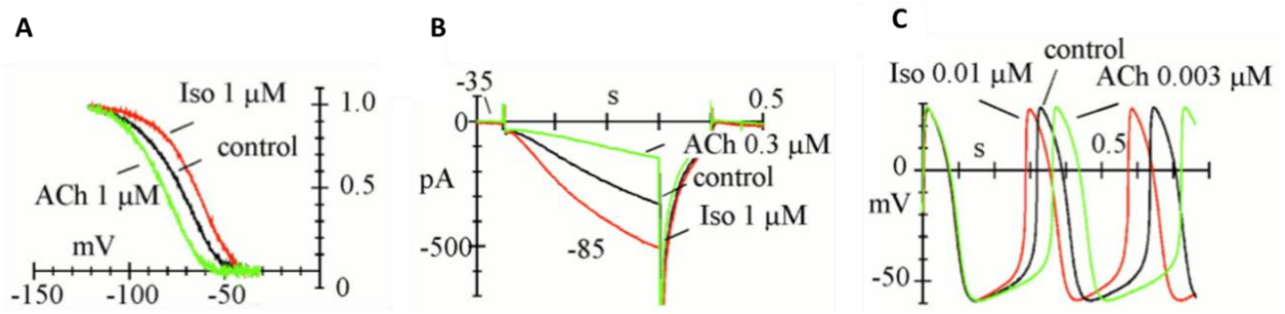

Figure 4. Effects of autonomic agonists on SAN spontaneous activity. Acetylcholine (ACh) and isoprenaline (Iso) induce a shift of the activation I_f curve to more negative/positive voltages, respectively (**A**). As consequence of these shifts the I_f current amplitude decreases/increases (**B**). The final effect of the autonomic agonist administration is deceleration (ACh) or acceleration (Iso) of spontaneous rate of action potentials (**C**). (From Accili et al., 2002[17])

HCN channels

The molecular correlates of the I_f current are the Hyperpolarization-activated Cyclic Nucleotide-gated (HCN) channels which belong to the superfamily of voltage gated potassium channels (Figure 5)[18,19]. They have a tetrameric form with each subunit composed by six transmembrane segments; the S4 is positively charged and acts as a voltage sensor; the pore is located between the S5-S6 loop; a Cyclic Nucleotide Binding Domain (CNBD) is localized in the C-terminus. Four HCN channel isoforms were cloned in mammals (HCN1-4) and their amino acid sequences are 80-90% identical in the core transmembrane regions and in the CNBD but diverge in the amino- and carboxy-terminal cytoplasmic regions.

All the isoforms share common characteristics: 1) activation by hyperpolarization; 2) mixed Na^+ and K^+ permeability (named I_f in the heart and I_h in the brain); 3) block by Cs^+ ; 4) direct modulation by cAMP; this molecule binds to the CNBD, and regulates the HCN open probability[17].

The four HCN isoforms differ quantitatively in the kinetics properties and in cAMP modulation. HCN1 has the fastest kinetics followed by HCN2 and HCN4; HCN1 has also the most positive half-activation ($V_{1/2}$) value while HCN4 and HCN2 display a more negative value. HCN1 is less responsive to cAMP, with a shift of 2-6mV, compared to HCN2 and HCN4 (shift: +10/+25mV)[20,21]. HCN3 shows time constant values between those of HCN4 and HCN2 and a $V_{1/2}$ similar to that of HCN1; interestingly its modulation by cAMP is very low[22] .

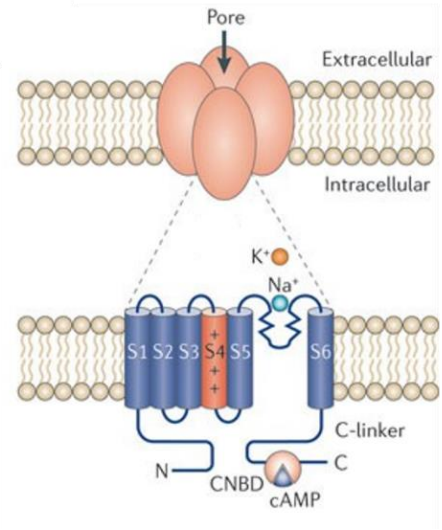

Figure 5. HCN channel structure. The channels are tetramers (upper panel). Each one of the four domains is composed of 6 transmembrane segments (S1–6) (lower panel). S4 is the voltage sensor domain. S5 and S6 form the conducting pore. In the C terminus the channel holds a cyclic nucleotide-binding domain (CNBD). (Modified form Postea and Biel 2011[23])

The L-Type and T-Type calcium currents

In cardiac cells it is possible to distinguish between two classes of voltage dependent calcium currents (I_{CaL} and I_{CaT}) Figure 6.

- the long lasting calcium current, called $I_{CaL,}$ is activated in depolarization (~40 mV), presents large single channel conductance, it is inhibited by calcium antagonist drugs (dihydropyridines, phenylalkylamines, and benzothiazepines) and, most important, it has a slow voltage dependent inactivation and therefore is named long lasting. In non-spontaneous cells I_{CaL} has a principal role in keeping the plateau phase of the AP therefore triggering the release of calcium from the intracellular stores and thus leading the excitation-contraction coupling. In SAN cells it is important in both the diastolic depolarization and upstroke phase.

- the transient calcium current (I_{CaT}) is activated in depolarization at more negative potential (~60 mV) compared to I_{CaL} and it is insensitive to the calcium antagonist drugs. It is called transient because it holds a rapid voltage dependent inactivation and, as expected from its functional properties, I_{CaT} is activated in the diastolic depolarization phase of the SAN AP influencing the rhythmic firing[24].

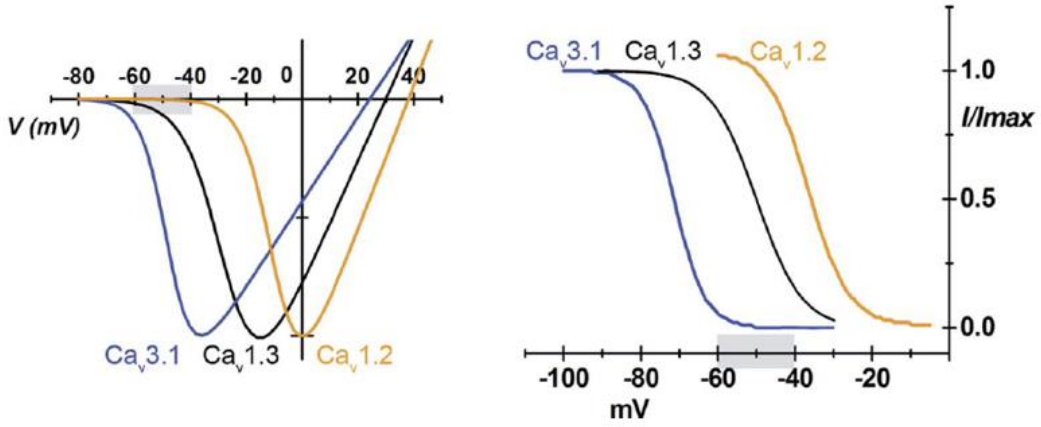

Figure 6. Voltage dependent calcium current. Current-voltage relation (left) and inactivation curve (right) of two kinds of I_{CaL} channel ($Ca_V1.3$ and $Ca_V1.2$) and one I_{CaT} channel (Ca_V 3.1) expressed in SAN. (From Mangoni and Nargeot 2008[13])

Voltage gated calcium channels

Voltage gated calcium channels are constituted by a protein complex formed by five different subunits: α1 (approximately 170 kDa), α2 (approximately 150 kDa), β (approximately 52 kDa), δ (approximately 17–25 kDa), and γ (approximately 32 kDa)[25](Figure 7).

The transmembrane α1 subunit is the principal component of the complex and it is organized in four repeated domains (I–IV), each containing six transmembrane segments (S1–S6). The S4 segment is the voltage sensor, while the S5-S6 structure forms the pore of the channel[26]. The β subunit is an intracellular protein that binds to the loop between domains I and II of the α1 subunit; the δ subunit is a glycoprotein with four transmembrane segments; the α2 is an extracellular extrinsic membrane glycoprotein that assembled with δ subunit binds to the extracellular membrane[25].

The accessory subunits regulate the level of expression and modulate the gating properties of the channel[26].

Three macro groups of voltage gated calcium channel can be identified based on the differences among the α1 subunits: Ca_V1, Ca_V2 and Ca_V3. The Ca_V2 channels give rise to P-type and Q-type

currents that were identified in neurons while the Ca_V1 and the Ca_V3 conduct the L-Type and the T-Type calcium currents, respectively[26].

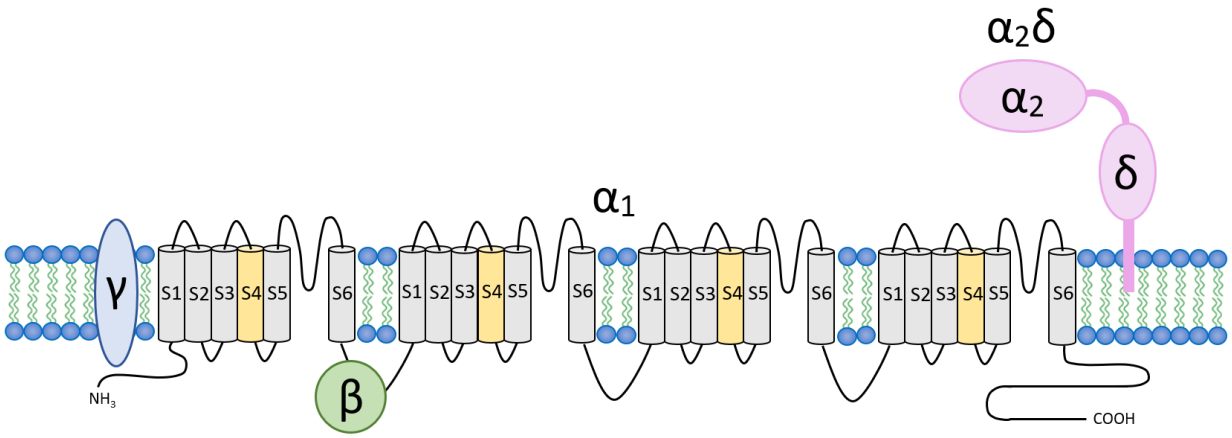

Figure 7. Voltage gated calcium channel structure. The accessory subunits α2-δ, β and γ interact with principal subunit α1; α1 is constituted by 4 domains each one formed by 6 transmembrane segments (S1–6). S4 is the voltage sensor. S5 and S6 form the conducting pore.

Calcium Clock

Intracellular Ca^{2+} cycling has been demonstrated to be a fundamental contributor to SAN automaticity. Indeed, to date it is known that the Ca^{2+} release from the sarcoplasmic reticulum (SR) is important in regulating pacemaker activity of SAN cells; this mechanism has been named calcium clock (**Figure 8**).

Briefly, the SR rhythmically releases Ca^{2+} ions through the ryanodine receptors (RYRs), in a spontaneous or $Ca_V1.3$ induced manner[11,12]. Ca^{2+} ions are then in part brought out of the cell thanks to the sodium-calcium exchanger (NCX) that extrudes 1 Ca^{2+} in exchange for 3 Na^+ ions generating a depolarizing current (I_{NCX})[14]; the Ca^{2+} cycling is assured by the activity of SERCA (Sarcum Endoplasmic Reticulum Calcium-ATPase) pumps, located on the membrane of the SR membrane, which bring back in the SR the majority of the Ca^{2+} ions.

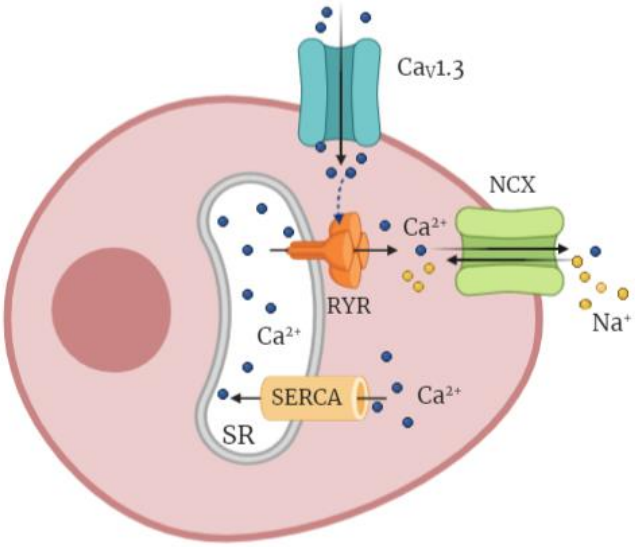

Figure 8. Calcium clock. SR rhythmically releases Ca^{2+} ions through the RYRs, in a spontaneous or $Ca_V1.3$ induced manner. Released Ca^{2+} ions are squeezed out from the cell thanks to the NCX that extrudes1 Ca^{2+} in exchange for 3 Na^+ ions generating a depolarizing current. The preservation of the Ca^{2+} cycling is assured by the SERCA pump.

SAN Automaticity extrinsic control

SAN automaticity needs to respond to extrinsic physiological demand. The basal heart rate (HR) results, therefore, from the regulation of the SAN intrinsic heart rate through neurohumoral system[27]. This complex control is mainly exerted by the Autonomic Nervous System (ANS) and several circulating or locally released factors (i.e. hormones).

Autonomic control of heart rate

The ANS is constituted by two branches: the parasympathetic nervous system (PNS) and the sympathetic nervous system (SNS), both innervating the different parts of the heart, including the conduction system (Figure 9).

The SNS releases catecholamines which bind to β-receptors and cause an increase in the production of the intracellular cAMP concentration by adenylate cyclase, a process mediated by a stimulatory Gs protein. cAMP acts as a second messenger increasing the activity of the Protein Kinase A (PKA) which, in turn, phosphorylates several proteins on the membrane, such as the L-type Ca^{2+} channels[28].

In addition, cAMP increases the opening chance of HCN channels by direct binding to them in a PKA-independent way [16].

Finally, catecholamines cause: increase of SAN rate, rise of the impulse conduction and general excitability and increase of the atrial and ventricular force of contraction.
The PNS releases acetylcholine with opposite effects to those of SNS causing two main effects on the heart: decrease of SAN rate and reduction of AVN fibers excitability, slowing down impulse transmission.

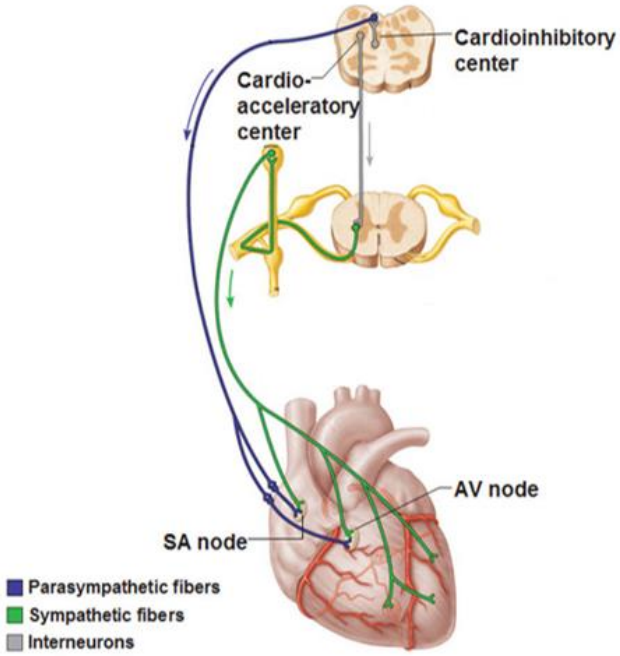

Figure 9. Autonomic innervation of the heart. The ANS, constituted of the parasympathetic and the sympathetic branch, innervates different parts of the heart.

Hormonal control of the heart rate

Many different molecules acting as autocrine, paracrine or endocrine factors have been identified to regulate the HR[27].
For example, it is well understood that in human the thyroid hormones are involved in regulation of the heart frequency. Moreover, Parathyroid Hormone (PTH) has been shown to increase the AP frequency in rabbit SAN myocytes increasing the I_f current density[29] and in clinical study a positive correlation between PTH levels and HR is emerged[30].
Additionally, the inflammation has been identified as an element that can regulate the HR. Indeed, Bradykinin, an inflammatory mediator, has been demonstrated to cause a depolarizing shift of HCN channels in rabbit SAN myocytes that is expected to increase the HR[31].
Therefore, there is several evidence that the extrinsic SAN automaticity regulation is not limited to the ASN supervision but a multitude of neurohormonal factors occurs.

FGF family

The Fibroblast Growth Factor (FGF) family gathers a wide number of proteins characterized by a common core sequence (140 amino acid) that are involved in several and various functions both in the adult organism and during development. At the cellular level, secretions of FGFs regulate essential processes among which regulation of proliferation, survival, migration, differentiation and metabolism[32].

The human/mouse FGF gene family includes 22 members, named from FGF1 to FGF23 (**Figure 10**). Nevertheless, since in vertebrates FGF15 and FGF19 are orthologs, in mice the molecule encoded by this sequence is usually referred as FGF15[33].

- FGFs can be classified in two major groups: secreted signalling proteins and intracellular non-signalling proteins. Intracellular non-signalling proteins (or iFGFs) are regulators of neuronal and myocardial excitability, interestingly they directly interact with the cytosolic carboxy terminal tail of voltage gated sodium channels (Na_V family) regulating their subcellular localization. Since these molecules do not leave the cytosol, they do not interact with any FGF receptor[34].
- Secreted FGFs operate their function outside the cell and it is possible to distinguish between canonical FGFs, that function as autocrine or paracrine factor, and endocrine FGFs.
  Canonical FGFs make their action through the binding with the FGF receptor complex, a transmembrane structure composed by a tyrosine kinase FGF receptor (FGFR) and a heparin/heparan sulphate cofactor.
  Endocrine FGFs operate their biological functions binding to the same receptors, however, due to their low affinity for the heparin/heparan sulphate cofactor, they require to interact with a molecule that belongs to the Klotho family[34].

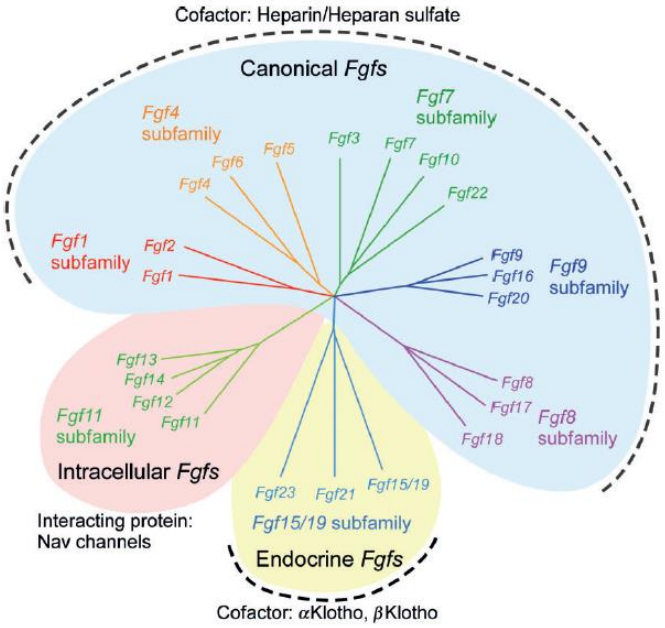

Figure 10. FGF families. Phylogenetic analysis suggests that 22 FGFs can be arranged into 7 subfamilies and three major groups: intracellular FGFs, canonical FGFs and endocrine FGFs. (From Ornitz and Itoh, 2015[34])

FGFR

FGFRs are tyrosine kinase receptors which display an extracellular binding structure composed of three immunoglobulin-like domains (D1-D3), a transmembrane helix segment and an intracellular kinase domain, as shown in Figure 11.

This receptor family consists of four members: FGFR1-4; however, since FGFR1, 2 and 3 exist in two alternative splicing variants (which differ in the last part of the D3 domain) it is possible to list a total of seven FGFRs: FGFR1b, 1c, 2b, 2c, 3b, 3c, and 4.

The ligand, binding to the extracellular portion of the receptor, causes the dimerization of the FGFRs and the trans-autophosphorylation of specific intracellular tyrosine residues which lead to the activation of various downstream pathways[35].

The four isoforms are ubiquitously expressed both in humans and mice. FGFR1 and FGFR2 are the most widespread isoforms[36].

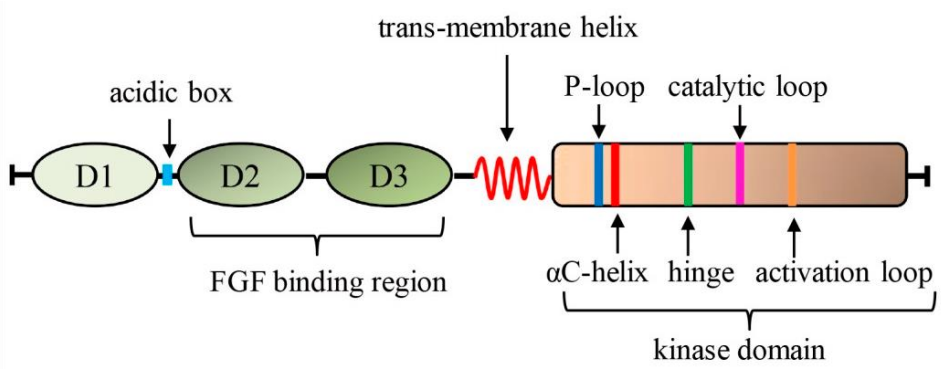

Figure 11. Schematic representation of FGFR. FGFR are composed of three immunoglobulin-like domains (D1-D3), a transmembrane helix segment and an intracellular kinase domain

α-KLOTHO

The Klotho gene was identified in 1997 by M. Kuro-o and his group as an aging-suppressor factor[37] and for this reason they decided to call it "Klotho", as the Greek goddess that spins the thread of human life in Greek mythology. Accordingly, α-Klotho KO mice display a phenotype that resembles human aging[37].

There are four different forms of α-Klotho: the full-length transmembrane form, two soluble forms and a secreted form (Figure 12). The full-length transmembrane form is composed by two extracellular glycosyl hydrolase domains, KL1 and KL2, and binds to the FGFR increasing the affinity of FGF23 for the FGFR-complex. The soluble forms derive from two different cleaving processes mediated by two secretases (ADAM10 and ADAM17) and the β-secretase β-APP cleaving enzyme 1 (BACE1). Their action can generate a 130 kDa soluble α-Klotho protein constituted only by the extracellular KL domains (through an α-cut on the full protein) or a 65 kDa structure characterized by the presence of the only KL1 domain (through a β-cut on the soluble form previously described). The secreted form of α-Klotho derives from an alternative RNA splicing event that generates a short and secreted form of α-Klotho constituted by the only KL1 domain; this form is very similar to the 65 kDa soluble one derived from the β-cut. Both the soluble and the secreted forms of α-klotho circulate in the blood flow and act as hormones[38].

The expression of the full-length α-Klotho protein is limited to kidneys, parathyroid gland, brain and some arteries[39]. However, single mutations in the Klotho gene cause extensive systemic aging phenotypes. This apparently strange situation can be explained by the existence of the circulating forms which are essential for the correct functioning of other organs.

The transmembrane form of α-Klotho principally operates as a coreceptor of FGF23, therefore acting in the regulation of the mineral metabolism (see next session). On the other hand, the circulating forms (soluble and secreted) of α-Klotho could act as a hormone exerting pleiotropic action including the regulation of several ion channels and calcium handling protein[40,41,42,43]. Interestingly,

α-Klotho circulating forms directly regulate the functions of cardiac myocytes exerting a cardioprotective role (see paragraph "α-Klotho cardioprotective role").

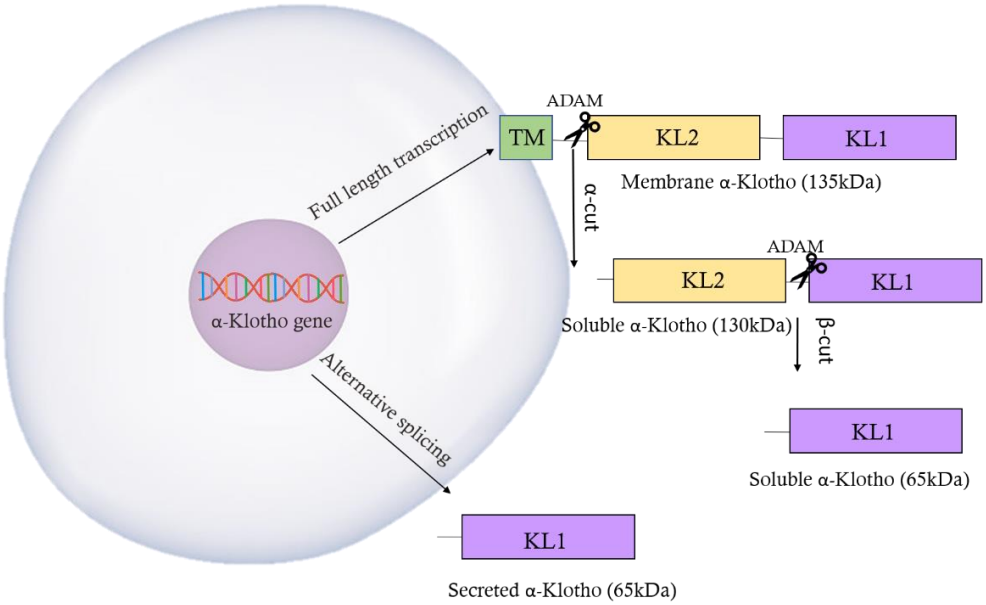

Figure 12. Different α-Klotho forms. Two soluble α-Klotho forms originate from the cleavage of the transmembrane α-Klotho. The secreted α-Klotho derives form an alternative splicing process.

FGF23

FGF23 is a 32 kDa glycoprotein that, together with FGF21 and FGF15/19, is a member of the endocrine FGF subfamily. Under physiological conditions it is predominantly produced by osteoblasts and osteocytes in order to regulate the mineral metabolism[44]. It can bind to all FGFRs (with a preference for FGFR1c) through a domain located in its N-terminal region, but the presence of α-Klotho increases FGF23 affinity for the receptor of about 20 folds[2].

FGF23 Renal Action

The canonical role of FGF23 is to regulate phosphate and vitamin D homeostasis. It is well established that the binding of FGF23 to the FGFR-α-Klotho complex in the proximal renal tube activates a signalling cascade involving ERK1/2 and SGK1. This process leads to the phosphorylation of the Na^+/H^+ exchange regulatory cofactor (NHERF)-1 which, in turn, releases the membrane cotransporters NaPi-2a and NaPi-2c which are then internalized and degraded. This action is similar to the one of the parathyroid hormones (PTH); indeed, also PTH suppresses the membrane expression of NaPi-2a and NaPi-2c in renal proximal tubules in the same way as FGF23. The ultimate effect of these processes is to increase the urinary phosphate excretion[1] (Figure 12).

Another important function of FGF23 is to regulate vitamin D level. In renal proximal tubules FGF23 is able to suppress the expression of the 1α-hydroxylase through a FGFR- α-Klotho dependent mechanism, that activates the ERK1/2 pathway which in the end causes the decrease of the vitamin D active form. Although this process is accepted, the molecular mechanism downstream ERK activation is currently unknown[1] (**Figure 13**).

FGF23 acts also on the distal nephron where it increases sodium and calcium reabsorption. In this scenario, FGF23 works as sodium-conversing hormone enhancing the sodium-chloride channel (NCC) expression and activity through a FGFR-α-Klotho stimulation and the subsequent ERK1/2-SGK1-WNK4 signalling. This mechanism increases sodium retention that may contribute to hypertension and heart hypertrophy[45].

Furthermore, FGF23, through the activation of the FGR-α-Klotho/ERK1/2-SGK1-WNK4 pathway, increases the calcium channel Transient Receptor Potential Vanilloid-5 (TRPV5) expression in distal renal tubules thus rising renal calcium reabsorption[46].

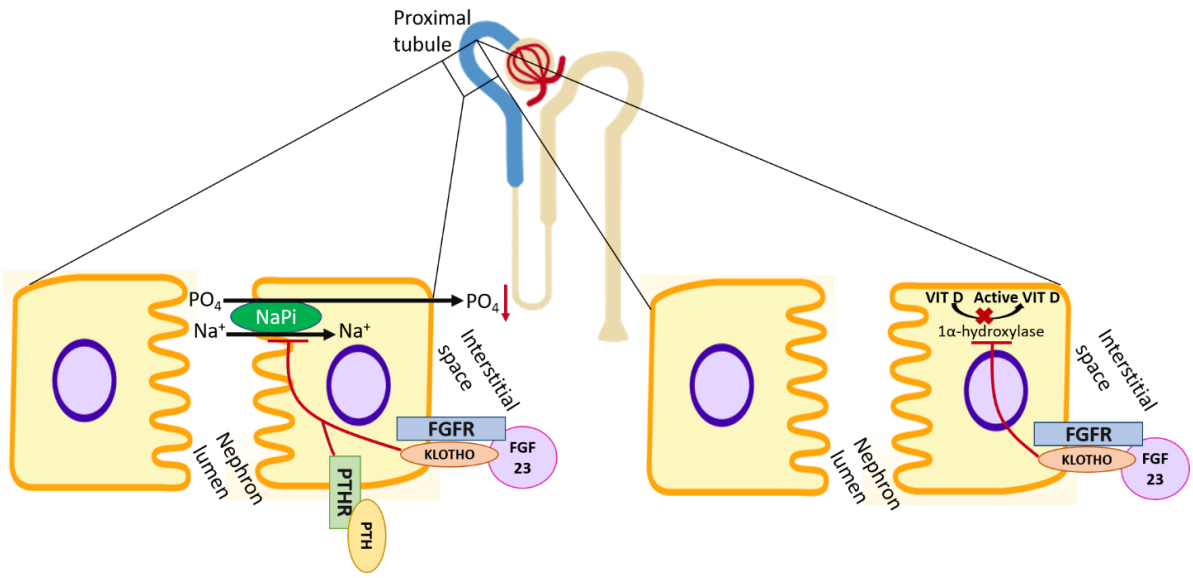

Figure 13. FGF23 renal action. In the renal proximal tubule FGF23 increases the phosphate excretion (left) and suppresses the production of the active form of vitamin D (right).

FGF23 Regulation of Production

The regulation of FGF23 production is a complex mechanism, still far from being fully understood. Many factors have been shown to increase FGF23 production, such as: vitamin D[47], PTH[48], dietary phosphate[48], AMP-activated kinase (AMPK) deficiency[49], iron deficiency[50] and pro-inflammatory cytokines[50] .

Despite several factors are involved in FGF23 regulation the most important modulator is Vitamin D. FGF23 and vitamin D form a classical hormonal feedback loop: an increase in Vitamin D levels causes an increment in FGF23 concentration that in turn suppresses Vitamin D production[47].
The importance of phosphate in the FGF23 regulation is small if compared with Vitamin D[33]. However, it is known that dietary intake of phosphate regulates FGF23 levels, but this effect seems to be a Vitamin D receptor (VDR) dependent mechanism; indeed, in VDR KO mice dietary phosphate supplementation failed to induce FGF23 expression while in WT mice it causes an increase in FGF23 circulatory levels[51].
The PTH-induced increase in FGF23 expression is well established; Meir and colleagues reveal that PTH increases the FGF23 production activating the orphan nuclear receptor Nurr1[52]. It is instead still unclear whether FGF23 downregulates PTH through a feedback loop since there are conflicting results on this point[33].

FGF23 and α-Klotho KO mouse models

Defects in α-Klotho or FGF23 gene expression cause very similar phenotype in mice and this observation supports the hypothesis that α-Klotho and FGF23 act in cooperation. α-Klotho and FGF23 heterozygotes mice did not show significant differences in general appearance and growth when compared to their WT littermates, while the homozygous mice show a reduced life span and prematurely die around 8-9 weeks of age. In contrast transgenic mice that overexpress α-Klotho live longer compared to WT mice[53].
Both α-Klotho$^{-/-}$ and FGF23$^{-/-}$ show: atrophy of genital organs and infertility; size reduction of thymus; defects in bone development with decreased mineralization; increased levels of circulating vitamin D, phosphate and calcium; hypoglycaemia; cardiac hypertrophy and fibrosis; ectopic calcification in gastric mucosa, trachea, blood vessels, and renal tubules[54-56]. Ectopic calcification in α-Klotho deficient mice may be secondary to elevated blood calcium, phosphate, and vitamin D levels[57]. Moreover α-Klotho$^{-/-}$ mice display intrinsic bradycardia and die after restrain stress for sinus arrest[3]. Because of this phenotype hypomorphic Klotho represents one of the best mammalian models for premature-aging syndromes[37].
Despite α-Klotho$^{-/-}$ and FGF23$^{-/-}$ mice present a very similar phenotype they display enormous differences in FGF23 serum levels. As expected FGF23$^{-/-}$ mice have undetectable levels of circulating FGF23[58] whereas α-Klotho$^{-/-}$ mice show huge FGF23 plasma levels compared with WT mice[40].
Interestingly Hesse and colleagues generate a VDR-FGF23 double mutant mouse that is a phenocopy of VDR mutant mouse only, thus rescuing the principal effect due to the lack of FGF23. This result suggests that the phenotype of FGF23$^{-/-}$ mice is mainly caused by excessive vitamin D signalling[59].

FGF23 and α-Klotho disorders in human

A primary excess of FGF23 is associated with the onset of various phosphate wasting syndromes, including autosomal dominant hypophosphataemic rickets (ADHR), X- linked hypophosphataemia (XLH) and autosomal recessive hypophosphataemic rickets (ARHR). In these pathologies FGF23 serum level is high, while active vitamin D levels are decreased resulting in an inadequate bone mineralization that is called rickets in children whereas in adult is named osteomalacia. The patients present bone pain and deformities of the extremities.

A decrease in FGF23 level causes a familial tumoral calcinosis (FTC) characterized by ectopic calcification[54].

Two patients with two different mutation in α-Klotho gene have been identified; the first patient presents a loss of function mutation of α-Klotho and developed symptoms of FTC[60].

The second is characterised by an increase in circulating α-Klotho levels due to a translocation that occurs near α-Klotho gene. The patient also presents increased FGF23 and PTH blood levels that cause the onset of hypophosphatemic rickets[61].

A secondary excess of FGF23 blood levels is present in patients with chronic kidney disease (CKD); this pathology is characterized by a progressive decrease in the number of functional nephrons that in turn causes a decrease in phosphate excretion. To counterbalance the increased level of serum phosphate a rise of circulating FGF23 levels occurs followed by a decrease in vitamin D and an increase in PTH blood concentrations.

In the last stage of CKD, phosphate levels increase indicating a disruption of phosphate homeostasis due to an insufficient number of functional nephrons[62] (Figure 14).

CKD is known to be associated with an increased risk for cardiovascular (CV) mortality and morbidity and, as better explained in the paragraph "FGF23 heart action", FGF23 has been identified as the link between CKD and CV disease[56].

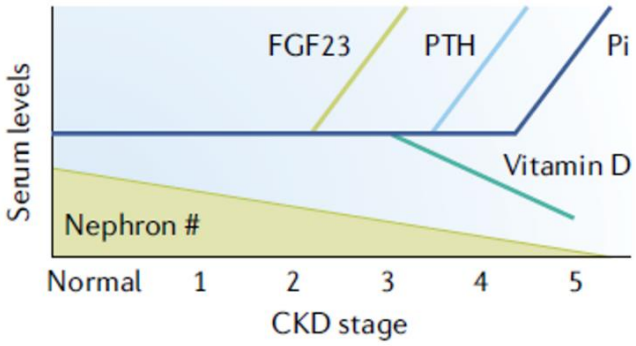

Figure 14.CKD progression. Schematic representation of the CKD development, serum variation of the principle molecules involved are represented.

FGF23-different activation pathway

FGF23 binding to FGFR activates two principal different signalling pathways. One is mediated by the phosphorylation of phospholipase Cγ (PLCγ) and the other is traduced by the FGF receptor substrate 2α (FRS2α).

FGF23 binding activates the FGFR causing the autophosphorylation of specific tyrosine residues of the receptor; when the Y766 residues is phosphorylated the PLCγ binds the FGFR to Y766 and the FGFR in turn phosphorylates and activates the PLCγ[63]. Activated PLCγ induces the production of (IP3) and diacylglycerol (DAG) from phosphatidylinositol 4,5-bisphosphate (PIP2); IP3 increases intracellular calcium ion levels and DAG activates protein kinase C (PKC)[64].

Opposite to PLCγ, FRS2α is constitutively bound to FGFR independently to FGFR activation; when FGFR is activated, it phosphorylates and activates FRS2α that once phosphorylated mediates the activation of Ras/mitogen-activated protein kinase (MAPK or ERK) and PI3K/Akt signalling[64].

Interestingly, as highlighted in Figure 15, in classic FGF23 target cells, that express α-Klotho, FGF23 predominantly activates the FRS2 α/ERK pathway, while in the absence of α-Klotho a prevalent activation of PLCγ pathway occurs[64].

Experiments carried out in HEK293 cells, that do not express endogenous Klotho, the FGF23 treatment induces a major activation of PLCγ pathway; nevertheless, a similar treatment in HEK293 cells overexpressing α-Klotho causes a signalling switch to the FRS2α/ERKcascade[65,66,67].

Remarkably the same effect has been observed when HEK293 cells were treated with soluble Klotho[68].

Furthermore, ventricular cardiomyocytes, that do not express α-Klotho, show a very low activation of FRS2α/ERK cascade compared to the PLCγ pathway[56].

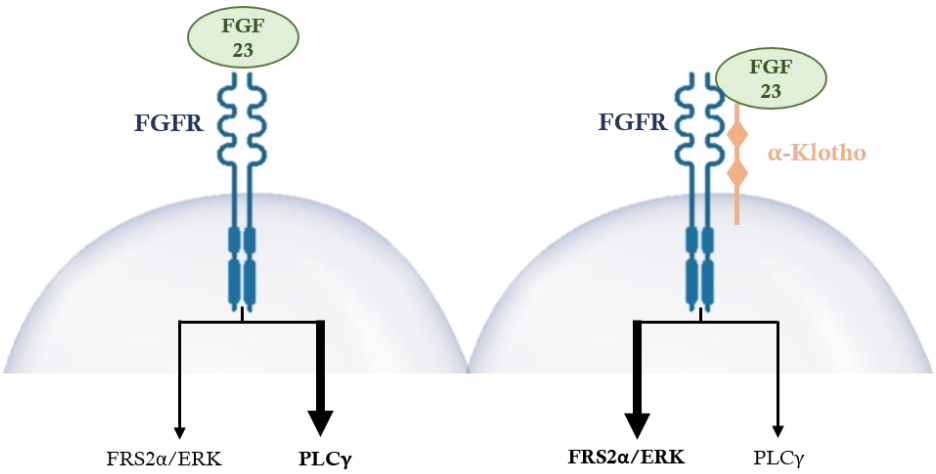

Figure 15. FGF23 activates different pathways. FGF23 triggers different signalling events depending on the availability of the co-receptor α-Klotho.

FGF23 Heart action

A variety of studies have shown the presence of FGF receptors in the working myocardium (atrial and ventricular cells) and functional studies have proven that FGF23 can affect function and structure of the myocardium; however at present it is not yet clear if the action of this hormone is limited to pathological states, such as cardiovascular diseases, or is also present during the normal physiological context[69].

FGF23 circulating levels are significantly increased in patients with CKD and strongly associated with CV diseases especially cardiac hypertrophy and arrhythmias[62]. Noteworthy, new insight suggests the high blood levels of FGF23 are associated with CV diseases also in patients that do not present impaired renal function[70,71].

Additionally, in experimental myocardial infarction, circulating FGF23 levels are increased; this rise depends not only on increasing production of FGF23 by bones but also by cardiomyocytes, suggesting a possible FGF23 paracrine role on the heart[72].

It has been described in literature and is generally accepted that, in the cardiac environment, FGF23 is able to induce hypertrophy and to modulate electrical and contraction activities of the heart with different time span.

Touchberry and colleagues[73] revealed that acute exposure of rat ventricular cardiomyocytes to FGF23 is able to increase intracellular calcium, due to higher I_{CaL} current, and to enhance ventricular muscle strip contractility. Navarro-Garcia and co-workers[74] demonstrate that FGF23 perfusion triggers pro-arrhythmic events in adult ventricular cardiomyocytes.

In rabbit pulmonary vein (PV) cardiomyocytes (the most important focus of atrial fibrillation onset), a 4-6 hrs treatment with FGF23 increases beating rate, sodium $I_{Na\text{-}Late}$ current and calcium transient[75].

HL-1 cardiomyocytes treated for 24hrs with FGF23 show increased L-type calcium currents, calcium transient, sarcoplasmic reticulum Ca^{2+} contents and enhance the incidence of delayed after depolarization[76].

After 48hrs of FGF23 incubation, hypertrophy has been detected in neonatal rat ventricular cardiomyocytes[56,65] and in HL1 cardiomyocytes[73].

A crucial point has been highlighted by Takeshita and colleagues[3]; they revealed that among the entire heart only the SAN expresses α-Klotho and, interestingly, α-Klotho KO mouse displays intrinsic bradycardia and dies after restrain stress for sinus arrest, thus suggesting that α-Klotho is essential for the normal activity of the SAN. Therefore, the SAN together with other few organs listed in previous section display α-Klotho expression. Taken together these results indicate that FGF23 could be a physiological regulator of the SAN activity.

α-*Klotho cardioprotective role*

A wide number of studies have displayed a cardioprotective role of the circulating α-Klotho forms[77,78].

In mice, treatment with α-Klotho exogenous protein after acute kidney injury prevents cardiac remodeling, preserves cardiac function and reduces hypertrophy and cardiac fibrosis[79]. Notably, it has been demonstrated that soluble α-Klotho ameliorates cardiac hypertrophy in mice overexpressing TRPC6 channel through downregulation of TRPC6 current in cardiomyocytes[77]. Another study performed in human cardiomyocytes and rat hearts has revealed that α-Klotho protein is released from cardiac tissue subjected to ischemic damage, moreover, in the same study it has been demonstrated that α-Klotho administration protects cardiomyocytes form ischemic damage increasing cells viability[78]. Huang and colleagues have demonstrated that the treatment with soluble α-Klotho significantly reduced spontaneous beating in rabbit PVs indicating a possible α-Klotho protecting role in atrial fibrillation onset[80].

Furthermore, patients with low soluble α-Klotho and high FGF23 serum present increase atrial fibrillation episodes[81].

Aim

Auto-rhythmicity regulation is a fundamental process to provide a stable HR and to allow an efficient and fast response to physiological demands.

The SAN intrinsic activity is indeed tightly regulated by a series of extrinsic mechanisms including the ANS and several molecules that act as endocrine autocrine and paracrine factors[27]. In this contest the proteohormone FGF23, a regulator of the mineral metabolism, appears to play an important role. In particular, the presence of α-Klotho, the specific FGF23 co-receptor, has been reported in the SAN tissue; furthermore, its absence leads to brady-arrhythmias episodes associated with sinus arrest or sinus block in α-Klotho KO mice[3].

Therefore, the aim of this project is to investigate the involvement of FGF23 in the maintenance and modulation of the electrical activity of mouse SAN cells and, hence, whether it can be considered new SAN activity regulator.

Results

Mouse Sinoatrial node analysis

We started our analysis investigating the expression of the FGFRs and their co-receptor α-Klotho in the SAN of WT mice.

We performed a reverse transcriptase quantitative PCR (RT-qPCR) analysis on two different cardiac murine tissues: SAN and Right Atrium (RA). In Figure 16A the mRNA levels of FGFR-complex, in SAN and RA, normalized with 18S housekeeping gene, are reported. These data disclose that membrane α-Klotho is more expressed in SAN than in RA while FGFR2, 3 and 4 are more present in RA than SAN ($p<0.05$). Among all FGFRs, FGFR1 is the most expressed in both SAN e in RA, both when normalized with 18s and α-actinin ($p<0.05$; One Way ANOVA, followed by Fisher test). Similar results have been obtained using α-actinin as housekeeping gene (Figure S1). Despite being not statistically significant, FGFR2 appears to be more expressed compared to FGFR3 and FGFR4 in SAN tissue ($p>0.05$; One Way ANOVA, followed by Fisher test). Thus, we decided to perform an immunofluorescence assay to investigate the protein expression of α-Klotho and FGFR 1 and 2 in SAN cells. As displayed in Figure 16B single SAN cells, identified from the shape and from the presence of HCN4 (green), a specific SAN cells marker[82], express α-Klotho (red, top), FGFR1 (red, middle) and FGFR2 (red, bottom).

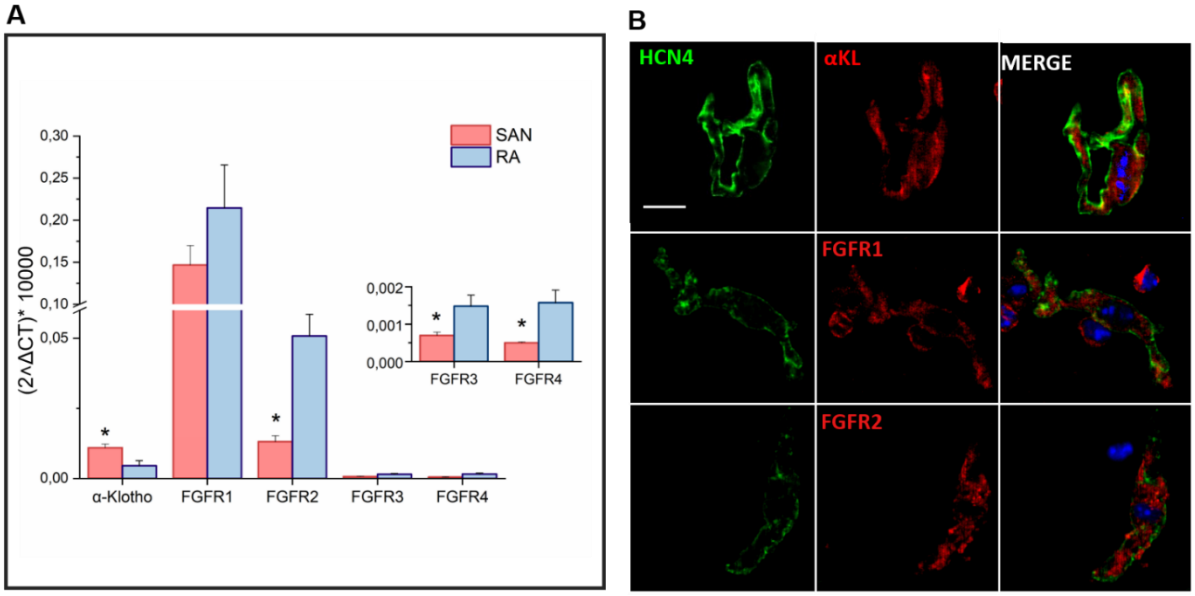

Figure 16. SAN cells express the FGFR-complex (α-Klotho, FGFR1 and FGFR2). (A) RT-qPCR analysis of α-Klotho and FGFR1-4 mRNAs in SAN and right atrium tissues normalized with 18S (n=3-4). The inset shows FGFR3 and FGFR4 expression data in an expanded scale. *, $p<0.05$ *vs* RA (Student's *t*-test). RA= Right Atrium. **(B)** SAN cells labelled with anti-HCN4 (green), anti-α-Klotho (red, top), anti-FGFR1 (red, middle) anti-FGFR2 (red, bottom) and overlapping of the 4 proteins (right, MERGE). Nuclei are stained with DAPI (blue). Scale bar 20μm.

Once confirmed that the SAN expresses the FGFR-complex, we started to evaluate the effect of FGF23 10 ng/mL on SAN electrical activity. We decided to test this FGF23 concentration since in literature the FGF23 *in-vitro* effects on cardiomyocytes were observed at several doses (from 0.1 ng/mL to 100 ng/m[73,74,75,76,56]); moreover FGF23 10ng/mL was also used to evaluate the *in-vitro* regulation of phosphate excretion in renal proximal tubules[80] (one of its physiological effect) . It has been described in literature and is generally accepted that, in the cardiac tissue, FGF23 is able to induce hypertrophy and to modulate the electrical and mechanical activity of the heart; however the time needed for the hormone to generate these effects span from few minutes to days[73,74,75,76,56] (see paragraph "FGF23 heart action" in the introduction for details). For this reason, we have investigated the FGF23 effects on murine SAN cells at different time points:

- After few minutes to study possible instantaneous effect.
- After 1 hr of incubation of the cells to analyse a possible short time effect.
- After 15 hrs of tissue incubation to examine a possible medium time effect.
- After 48hrs of tissue incubation to investigate the possible effect of a protracted exposure.

We first performed patch-clamp experiments perfusing FGF 23 10ng/mL directly on SAN cells to examine possible acute effects on their spontaneous activity, and on the I_f current, one of the main membrane clock components involved in the generation of SAN action potentials (APs)[16].
Time-courses and representative AP traces in the absence and in the presence of FGF23 10ng/mL recorded before (control, purple) and during FGF23 10ng/mL perfusion (orange) are shown in Figure 17A and B. Mean APs spontaneous rate was 6.0±0.34 Hz and 5.9±0.3 Hz (n=8) in the absence and in the presence of FGF23 respectively ($p>0.05$; Paired Student's *t*-test). Thus, no differences were observed in AP frequency when FGF23 was perfused on SAN cells. The effect of FGF23 on I_f current was evaluated by activating the current with a double voltage step protocol (-75mV/-125 mV, from an holding potential of -35mV) which allows to asses both changes in amplitude and voltage-dependence. Time-courses of I_f current amplitude measured at -75 mV in the absence and in the presence of FGF23 10 ng/mL, and sample current traces recorded before (control, purple) and during FGF23 10 ng/mL treatment (orange) are shown in Figure 17C, and D respectively. Mean current densities measured at-75 mV were 4.7±0.81 pA/pF, and 4.5±0.8 pA/pF (n=5) in the absence and in the presence of FGF23 10 ng/ml respectively ($p>0.05$; Paired Student's *t*-test). As expected, acute SAN cells exposure to FGF23 neither alters the amplitude nor the voltage-dependence of the I_f current.
Since no changes were observed on either AP rate or I_f amplitude during FGF23 perfusion, we ruled out the hypothesis of an acute effect of the FGF23 on SAN cells activity.

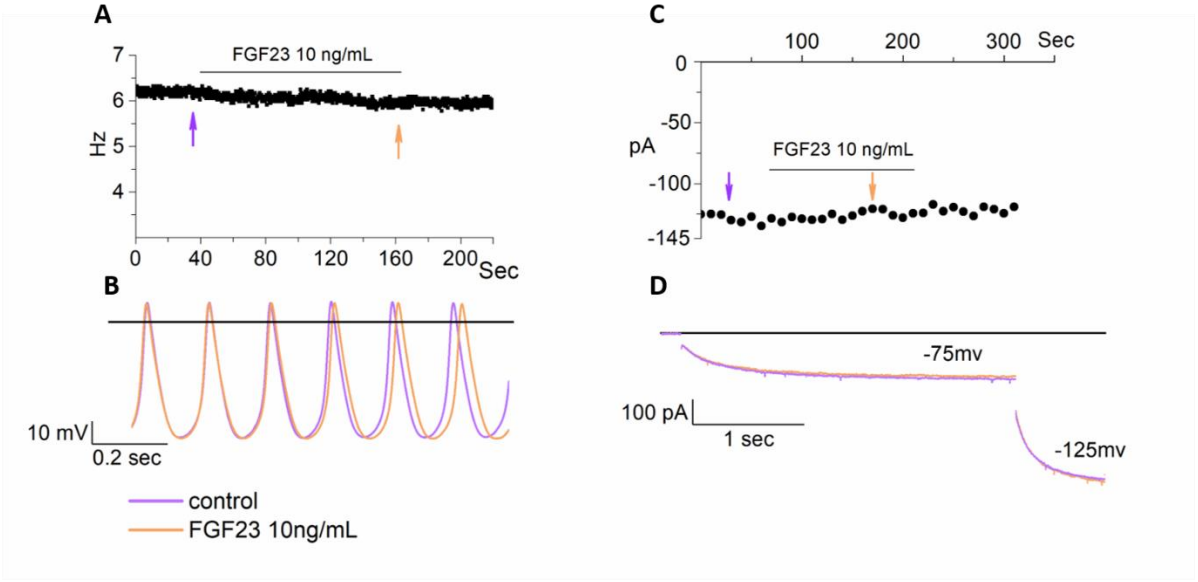

Figure 17. Acute exposure to FGF23 does not affect SAN cells electrical activity. (A) Time-course of AP frequency in the absence and in the presence of FGF23 10 ng/mL. **(B)** Representative action potential traces recorded before (purple) and during FGF23 10 ng/mL treatment (orange). **(C)** Time-course of the I_f current amplitude measured at -75 mV in the absence and in the presence of FGF23 10 ng/mL. **(D)** I_f current traces recorded at -75mV and -125mV as indicated (holding potential, -35 mV) before (purple) and during FGF23 perfusion (orange). Arrows in panel A and C represent the time at which traces in panel B or D were taken. The horizontal black line indicates the value of 0mV in **B** and 0 pA in **D**.

Similar results were obtained when freshly isolated SAN cells were incubated with either FGF23 10ng/mL or vehicle for 1 hr (**Figure 18**) or when the whole tissue was incubated for 15 hrs (**Figure 19**) before patch-clamp experiments.

Mean data of the AP rate in control and after 1hr of incubation with FGF23 (**Figure 18A**) clearly indicate that, even after 1hr exposure, FGF23 did not influence SAN spontaneous activity. The I_f current was elicited with a series of hyperpolarizing steps followed by a step at-125 mV (see materials and methods for details) to allow the evaluation of the maximal conductance (g_{max}), the steady-state IV curves and the activation curves. As shown in **Figure 18** (panels **B**, **C**, and **D**) none of these parameters was affected by FGF23.

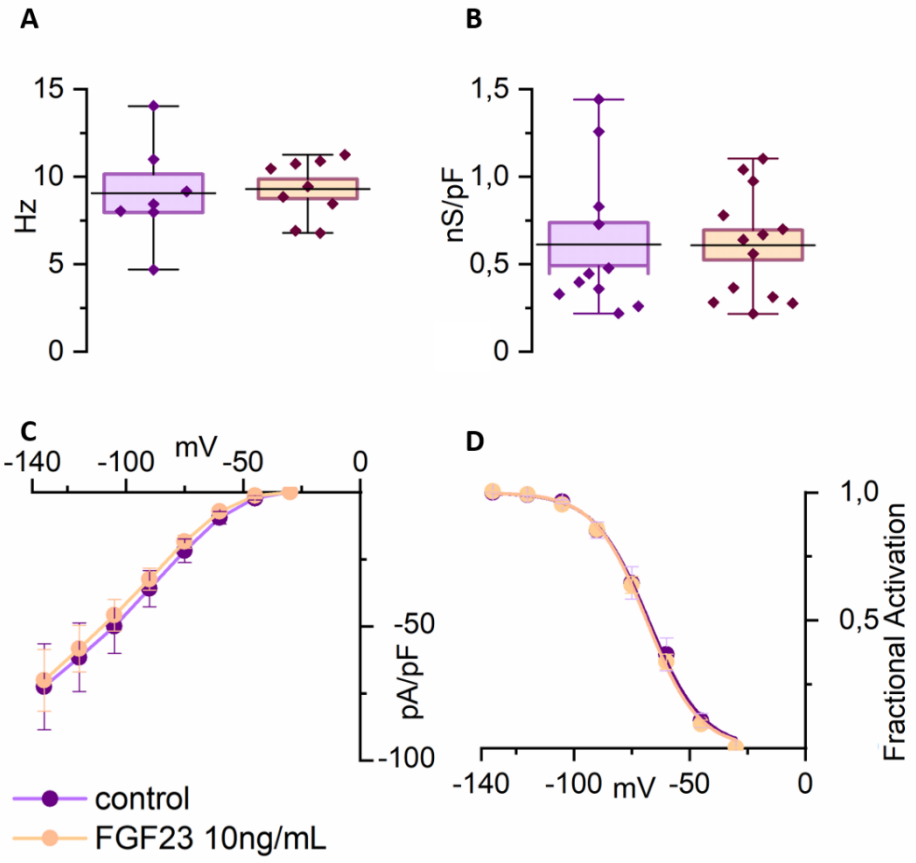

Figure 18. 1 hr FGF23 incubation has no effect on spontaneous activity of SAN cells. (A) Box plot of the AP rate indicated as mean (black line) ±SEM (box): control, 9±1.1 Hz (n=7); FGF23 10 ng/mL, 9.3±0.6Hz (n=9); the whiskers indicate the minimum and the maximum value. **(B)** Box plot of I_f maximal conductance (g_{max}) indicated as mean (black line) ±SEM (box): control, 0.61±0.12 nS/pF; FGF23 10 ng/mL, 0.61±0.09 nS/pF; the whiskers indicate the minimum and the maximum value. **(C)** Steady-state IV and **(D)** mean I_f activation curves; $V_{1/2}$ (mean±SEM): control, -67.4±2.8 mV (n=11); FGF23, -68.8±1.3 mV (n=13).

The mean AP rate in control and after 15hrs of incubation with FGF23 are illustrated in Figure 19A. The mean g_{max}, the mean steady-state IV curves and the mean activation curves of the I_f current, in control and after the 15 hrs of incubation with FGF23, are presented in Figure 19B and C and D respectively. Our data evidently show that FGF23 does not affect the electrical activity of SAN cells even after 15hrs of SAN tissue incubation.

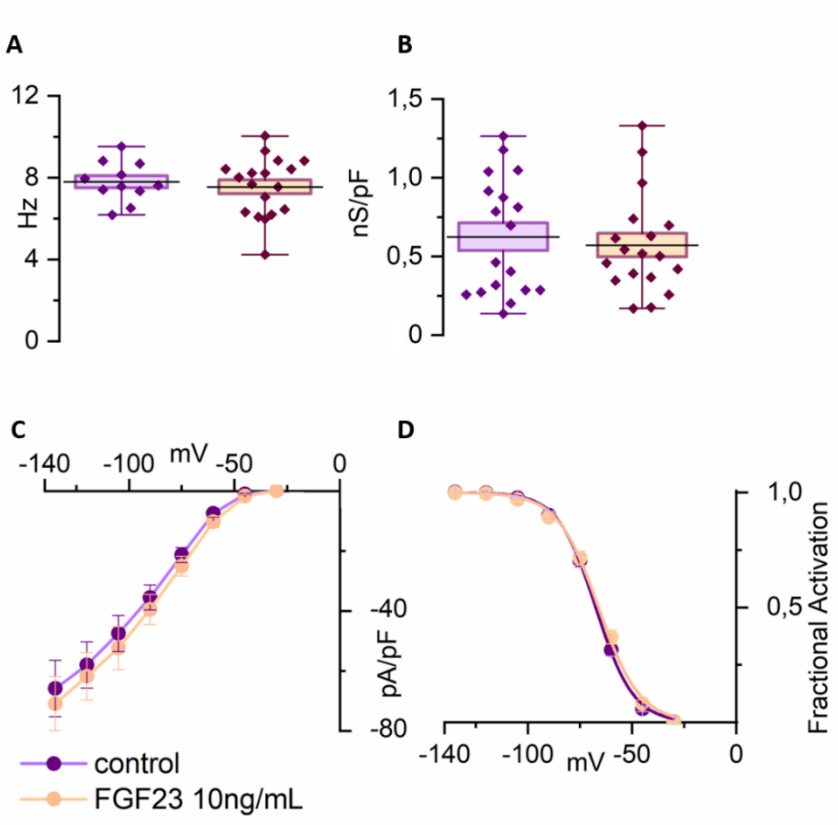

Figure 19. 15 hrs FGF23 incubation has no effect on spontaneous activity of SAN cells. (A) Box plot of the AP rate indicated as mean (black line) ±SEM (box): control, 7.8±0.3 Hz (n=11); FGF23 10 ng/mL, 7.5±0.3 Hz (n=18); the whiskers indicate the minimum and the maximum value. **(B)** Box plot of I_f maximal conductance (g_{max}) indicated as mean (black line) ±SEM (box): control, 0.62±0.14 nS/pF; FGF23 10 ng/mL, 0.57±0.1nS/pF; the whiskers indicate the minimum and the maximum value. **(C)** Steady-state IV and mean $I_f$current activation curves **(D)**, V1/2 (mean±SEM): control, -67.6±1.1 mV (n=18); FGF23, -66.1± 1.3 mV (n=18).

We then proceeded by evaluating the effects after 48 hrs of SAN tissue incubation with FGF23 10 ng/mL.

For this set of experiments, we maintained the SAN in culture for 48 hrs in the presence of either vehicle or FGF23 10 ng/mL. After the incubation, single SAN cells were isolated, and APs were recorded. Representatives AP traces recorded in the two conditions (control, purple; FGF23 orange), and mean AP rate values are shown in Figure 20A and B respectively. These data clearly indicate that FGF23 increases the spontaneous activity of SAN cells (control: 7.5±0.4 Hz; FGF23: 9.9±0.4 Hz. $p<0.05$). In addition, this effect was completely abolished when SAN tissue was incubated with both FGF23 10 ng/mL and the FGFR blocker PD173074 1μM (Figure 20), thus indicating that the AP frequency increase depends on the specific biding of FGF23 with the FGFR. Moreover, the incubation with the blocker alone does not have any significant effect on the spontaneous activity of SAN cells (Figure 20). The FG23-induced increase in APs frequency was abolished also by PD173074 100 nM but not by PD173074 10 nM (Figure S2).

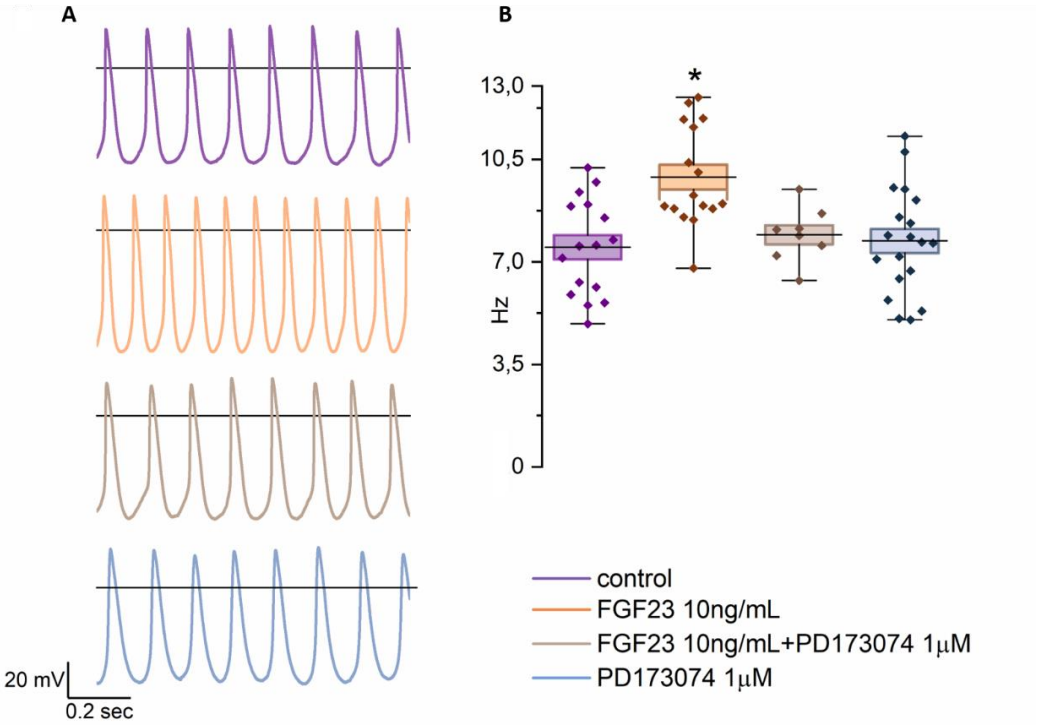

Figure 20. 48 hrs FGF23 10 ng/mL incubation increases the AP rate of SAN cells stimulating the FGFR. (A) Representative AP traces recorded after 48 hrs of incubation with vehicle (control; purple), FGF23 10 ng/ml (orange), FGF23 10 ng/mL+PD173074 1μM (brown) and PD173074 1μM (light blue). The horizontal black line represents the value of 0 mV. **(B)** Box plot of the AP rate indicated as mean (black line) ±SEM (box): control, 7.5±0.4 Hz (n=16); FGF23, 9.9±0.4 Hz (n=16); FGF23+PD173074 1μM 7.9±0.3 Hz (n=8); PD173074 1μM 7.7±0.4 Hz (n=19). the whiskers indicate the minimum and the maximum value. *, $p<0.05$ vs control, vs FGF23 10 ng/mL+PD173074 1μM, and vs PD173074 1μM treated cells (One Way ANOVA, followed by Fisher test).

In agreement with APs results we observed that FGF23 was able to increase the I_f current density after 48 hrs of incubation only in the absence of PD173074 1μM (**Figure 21**). Representatives I_f current traces recorded after 48 hrs of incubation with vehicle (control; purple), FGF23 10 ng/ml (orange), FGF23 10 ng/mL+PD173074 1μM (brown) and PD173074 1μM (light blue) are shown in **Figure 21A**. The mean g_{max} values obtained were control, 0.31±0.02 nS/pF; FGF23 10 ng/mL*, 0.42±0.03 nS/pF; FGF23+PD173074 1μM 0.31±0.02 nS/pF; PD173074 1μM 0.33±0.02 nS/pF (*. $p<0.05$ *vs* all the other conditions, **Figure 21B**). The mean steady-state IV curves are illustrated in **Figure 21C**. No effect of FGF23 was observed on channels voltage-dependence (**Figure 21D**). Since FGF23 48hrs treatment was shown to induce hypertrophy in ventricular myocytes and in HL1 cells[56,73] we additionally evaluated the effects of the incubation on the SAN cells capacitance and no differences were observed between the four conditions (One Way ANOVA, followed by Fisher test; data not shown).

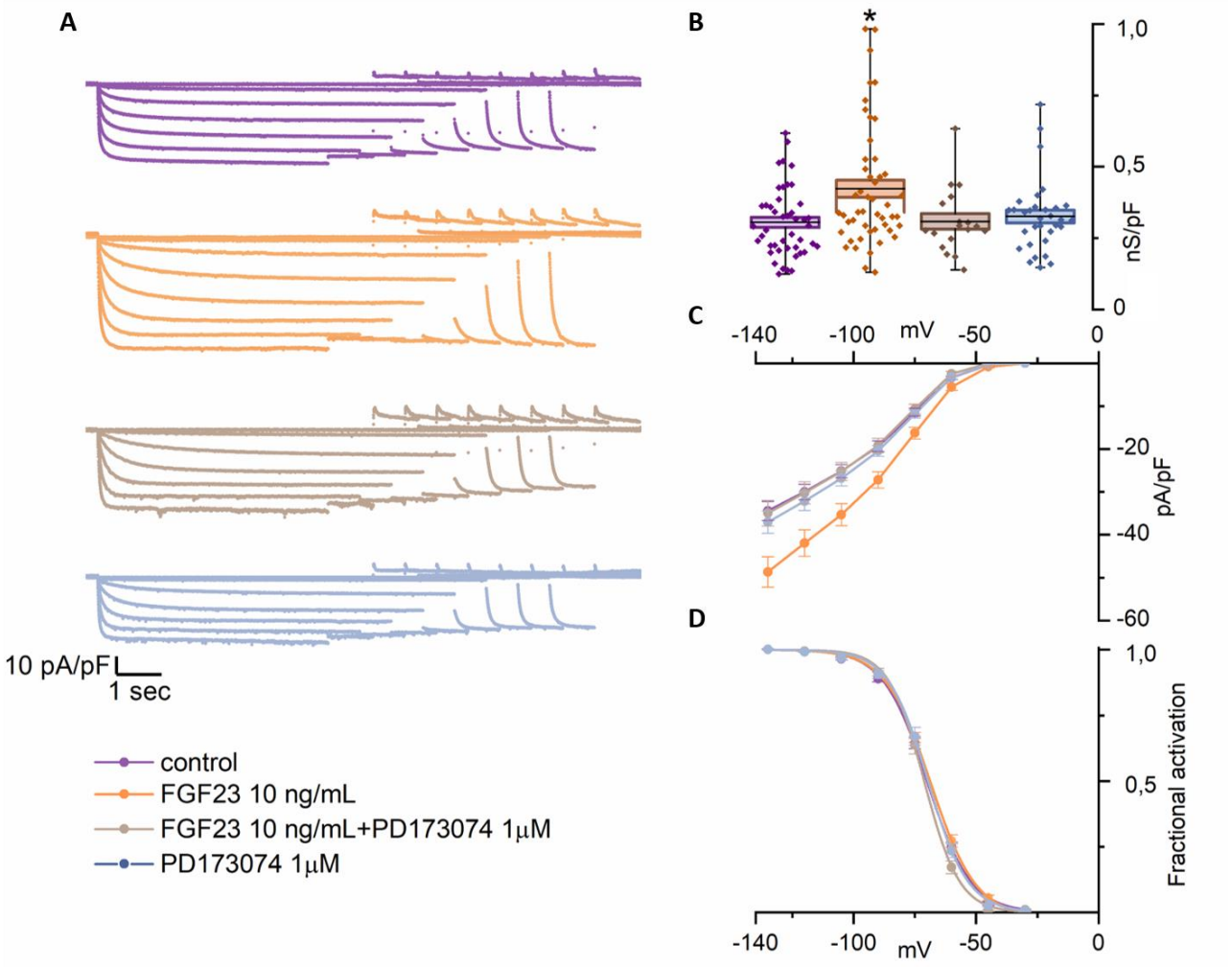

Figure 21. 48 hrs FGF23 10 ng/mL incubation increases the I_f current density of SAN cells stimulating the FGFR. (A) Representative I_f current traces recorded after 48 hrs of incubation with vehicle (control; purple), FGF23 10 ng/mL (orange), FGF23 10 ng/mL+PD173074 1µM (brown) and PD173074 1µM (light blue). **(B)** Box plot of I_f maximal conductance (g_{max}) indicated as mean (black line) ±SEM (box): control, 0.31±0.02 nS/pF; FGF23 10ng/mL, 0.42±0.03 nS/pF; FGF23+PD173074 1µM 0.31±0.02 nS/pF; PD173074 1µM 0.33±0.02 nS/pF. The whiskers indicate the minimum and the maximum value. Steady-state IV **(C)** and mean I_f activation curves **(D)**, $V_{1/2}$ (mean±SEM): control, -70.1±0.8 mV; FGF23 10 ng/mL,-68.5±0.8 mV; FGF23+PD173074 1µM -71.3±1.1 mV; PD173074 1µM -69.7±1.2 mV (n=45-49-18-32). *, p<0.05 vs control, vs FGF23 10 ng/mL+PD173074 1µM, and vs PD173074 1µM treated cells (One Way ANOVA, followed by Fisher test).

Another important current involved in auto-rhythmicity of SAN cells is the L-Type calcium current (I_{CaL})[24]; therefore, we checked for possible alterations in this current after 48 hrs of incubation with FGF23. The effect of FGF23 on I_{CaL} current was evaluated by applying specific voltage protocols to evaluate the IV curves, the activation and the inactivation curves (see materials and methods for details).

Mean I_{CaL} IV curves mean g_{max} and mean activation and inactivation curves are reported in Figure 22A, B and C respectively. Our data demonstrate that FGF23 48hrs incubation does not affect this current.

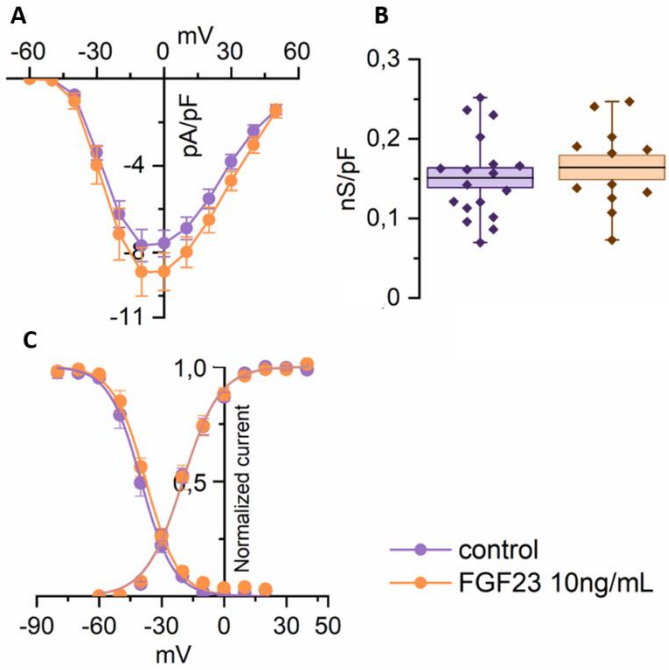

Figure 22. 48 hrs FGF23 10 ng/mL incubation have no effect on I_{CaL} current in SAN cells. **(A)** Mean steady-state IV curves **(B)** Box plot of I_{CaL} maximal conductance (g_{max}) indicated as mean (black line) ±SEM (box): control, 0.15±0.01 nS/pF (n=17); FGF23 10 ng/mL, 0.16±0.02 nS/pF (n=13). **(C)** mean activation and inactivation curves; Mean±SEM $V_{1/2}$ Inactivation values are: control, -39.8±0.32 mV (n=7); FGF23, -37.5±0.52 mV (n=9). Mean±SEM $V_{1/2}$ activation values are: control, -20±0.58 mV (n=17); FGF23, -19.9±0.46 mV (n=13).

Our results indicate that spontaneous activity of SAN cells can be affected by a long (48 hrs) exposure to FGF23, and in particular FGF23 increases the AP frequency, regulating the I_f current, through the binding with the FGFRs; however, the involvement of the co-receptor α-Klotho has not been fully clarified. Therefore, thanks to the collaboration with dr. G.Ruiz-Hurtado and dr. C. Delgado Canencia the effect of FGF23 on the I_f current was evaluated in SAN cells isolated from α-Klotho KO mice, a transgenic strain generated by prof. Makoto Kuro-o[37], and their littermates wild-type.

We started by evaluating the I_f current in freshly isolated SAN cells by using both a long IV protocol constitutes of 8 hyperpolarizing voltage steps and a short one of 4 hyperpolarizing voltage steps with a common step at -120 mV.

Representative I_f current traces, recorded with the 8 voltage steps protocol, form WT (blue) and α-Klotho KO mice (green) are presented in Figure 23A. Mean current density at -120 mV obtained from both the 8 and 4 steps protocol illustrated in Figure 23B are: WT, -27±2.5 pA/pF; α-Klotho KO, -19.5±2.1 pA/pF, ($p<0.05$). The mean steady-state IV curves and the mean activation curves acquired from the 8 voltage steps protocol are shown in Figure 23C and D respectively. These data indicate that α-Klotho KO mice present a decreased I_f current density compared with their WT littermates, that seemed to result from a change in maximal conductance and not in the voltage dependence. Furthermore, α-Klotho KO mice show a reduction in cell capacitance as illustrated in Figure 23E (WT: -31.3±1.4 pF; α-Klotho KO: -23.8±1.3 pF, $p<0.05$).

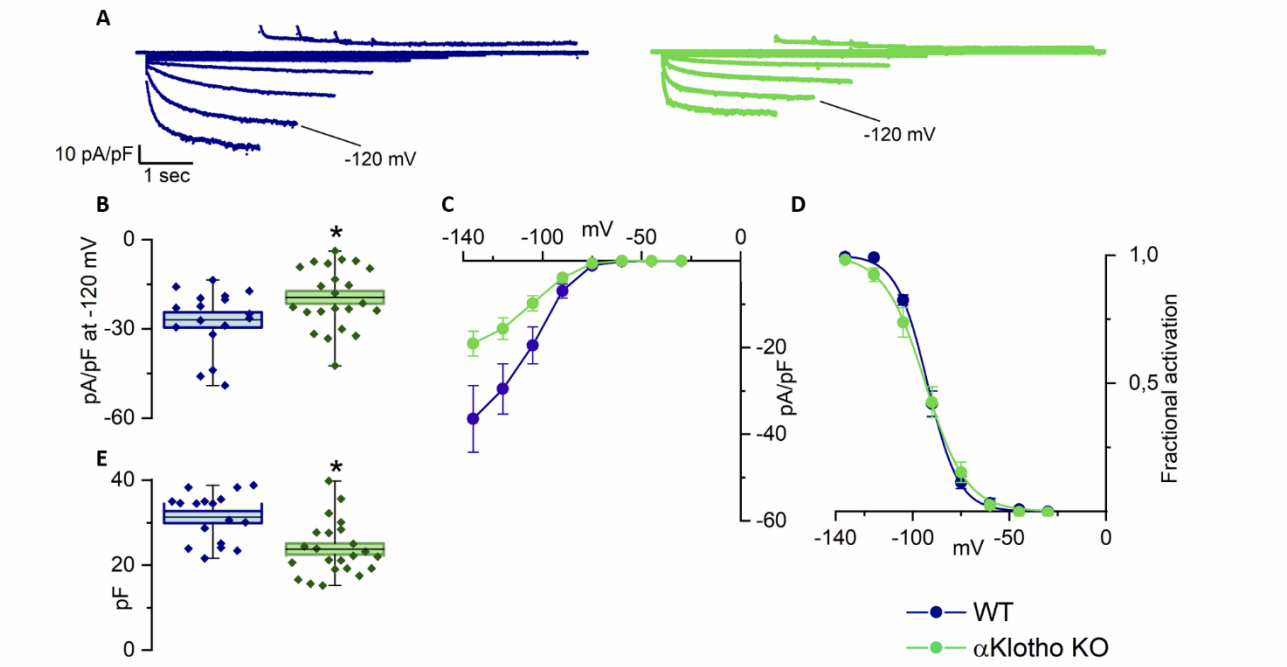

Figure 23. α-Klotho KO mice display a decreased I_f current density and capacitance. (A) Representative I_f current traces recorded form WT (blue) and α-Klotho KO mice (green). **(B)** Box plot of the I_f mean density at -120 mV indicated as mean (black line) ±SEM (box): WT, -27±2.5 pA/pF (n=17); α-Klotho KO, -19.5±2.1 pA/pF (n=23). The whiskers indicate the minimum and the maximum value. *, $p<0.05$ vs WT (Student's *t*-test). **(C)** Steady-state IV and **(D)** mean I_f activation curves, mean±SEM activation $V_{1/2}$ values: WT, -92.4±0.32 mV (n=6); α-Klotho KO, -93.5±0.33 mV (n=13). **(E)** Box plot of the mean cell capacitance indicated as mean (black line) ±SEM (box): WT, -31.3±1.4 pF (n=17); α-Klotho KO, -23.8±1.3 pF (n=23). The whiskers indicate the minimum and the maximum value. *, $p<0.05$ vs WT (Student's *t*-test).

These results appear to be in agreement with the evidence that α-Klotho KO mice display an intrinsic bradycardia[3] and thus its presence is fundamental for a normal activity of the SAN. Indeed, nevertheless α-Klotho KO mice display extraordinarily high FGF23 plasma level[40] they display a reduced I_f current density compared to WT.

To evaluate if α-Klotho is a necessary for the FGF23-mediated SAN activity modulation, we have investigated the ability of FGF23 to regulates the I_f current in the absence of α-Klotho. SAN tissues, isolated from WT and α-Klotho KO mice were incubated for 48 hrs with either vehicle or FGF23 10 ng/mL, and after cell isolation the I_f current was recorded. In Figure 24A representative I_f current traces at -120 mV from WT incubated in control (purple), WT incubated with FGF23 10ng/mL (orange), KO incubated in control (green) and KO incubated with FGF23 10ng/mL (red) are reported. Box plot of I_f mean current density at -120 mV are shown in Figure 24B. FGF23 tends to increase I_f current density in WT SAN cells (control: -27.5±3.8 pA/pF; FGF23 10ng/mL: -39.1±4.7 pA/pF, p=0.07), as previously well established by our experiments, but it has no effect on α-Klotho KO SAN cells (control: -34.5±7.7 pA/pF; FGF23 10ng/mL: -29.4±5.6 pA/pF). These data indicated that the FGF23 dependent increase of the I_f current is missing in the absence of α-Klotho, thus suggesting that the FGF23 acts on SAN cells via activation of FGFR- α-Klotho complex.

Capacitance of WT and α-Klotho KO SAN cells were compared after incubation in control and with FGF23 10 ng/mL; the results confirmed that the molecule does not alter this parameter ($p>0.05$; Student's *t*-test, data not shown). Therefore, we confronted the capacitance of WT FGF23 treated or not treated cells with KO FGF23 treated or not treated cells and as presented in Figure 24C, KO mice SAN cells display a decrease in capacitance compared with WT (WT: -29.1±1.8 pF; α-Klotho KO: -22.4 ±1.3 pF, $p<0.05$).

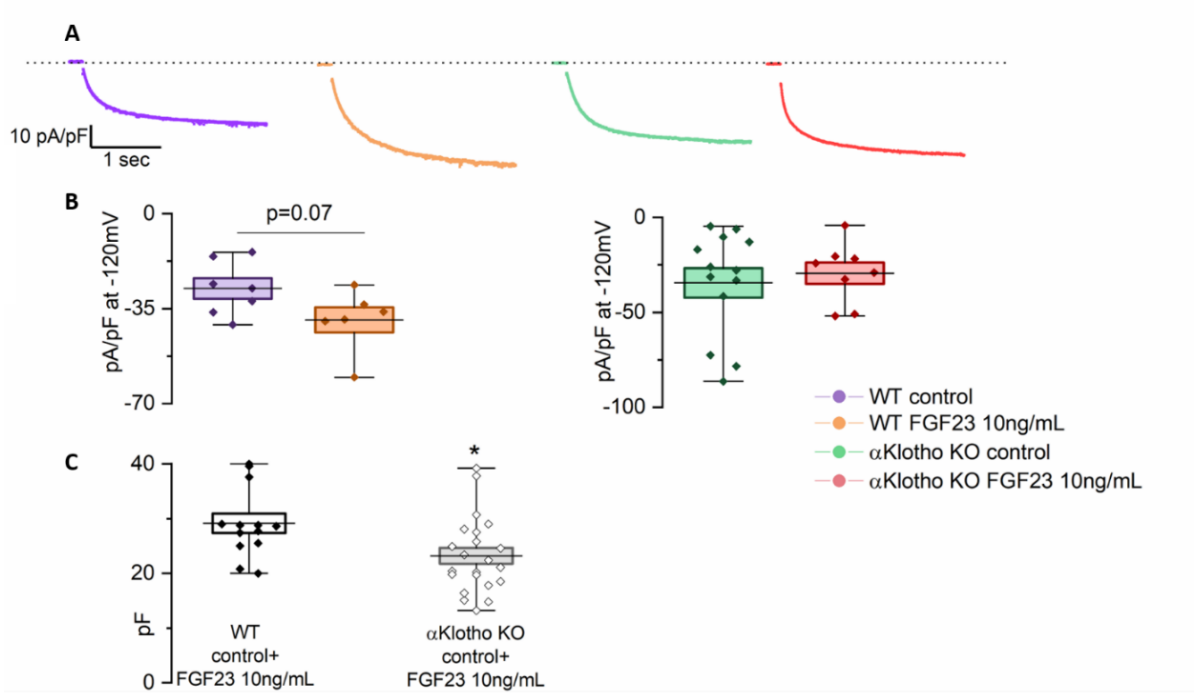

Figure 24. FGF23 48hrs incubation does not affect the I_f current density in α-Klotho KO mice.

(A) Representative I_f current traces at -120 mV recorded form WT in control (purple), WT in FGF23 10 ng/mL (orange), α-Klotho KO in control (green), α-Klotho KO in FGF23 10 ng/mL (red). The horizontal dotted line represents the value of 0 pA. **(B)** Box plot of the I_f mean density at -120 mV indicated as mean (black line) ±SEM (box): WT in control, -27.5±3.8 pA/pF (n=7); WT in FGF23 10ng/mL, -39.1±4.7 pA/pF (n=6); α-Klotho KO in control, -34.5±7.7 pA/pF (n=13); α-Klotho KO in FGF23 10ng/mL, -29.4±5.6 pA/pF (n=8). The whiskers indicate the minimum and the maximum value. p=0.07 WT in control vs in FGF23 10ng/mL (Student's *t*-test). **(C)** Box plot of the mean cell capacitance indicated as mean (black line) ±SEM (box): WT, -29.1±1.8 pF (n=13); α-Klotho KO, -22.4 ±1.3 pF (n=22). The whiskers indicate the minimum and the maximum value. *, p<0.05 vs WT (Student's *t*-test).

Lastly, since it was reported that FGF23 predominantly activates the FRS2 α/MAPK pathway in cells that express α-Klotho[65], we decided to investigate the ERK pathway in SAN cells after 48 hrs FGF23 treatment. In Figure 25A two Western Blot experiments that compared ERK and the phosphorylated form of ERK (pERK) after 48 hrs of incubation in control, with FGF23 10 ng/mL or in fresh tissue (no incubation) are reported. In Figure 25B the densitometric analysis of the chemiluminescent signal of pERK/ERK normalized on control condition (48hrs of incubation with vehicle) are shown.

Our preliminary results indicate that the pathway of ERK is highly activated in the fresh tissue; and FGF23 10ng/mL 48 hrs treatment increase the phosphorylation of ERK compared with vehicle incubation.

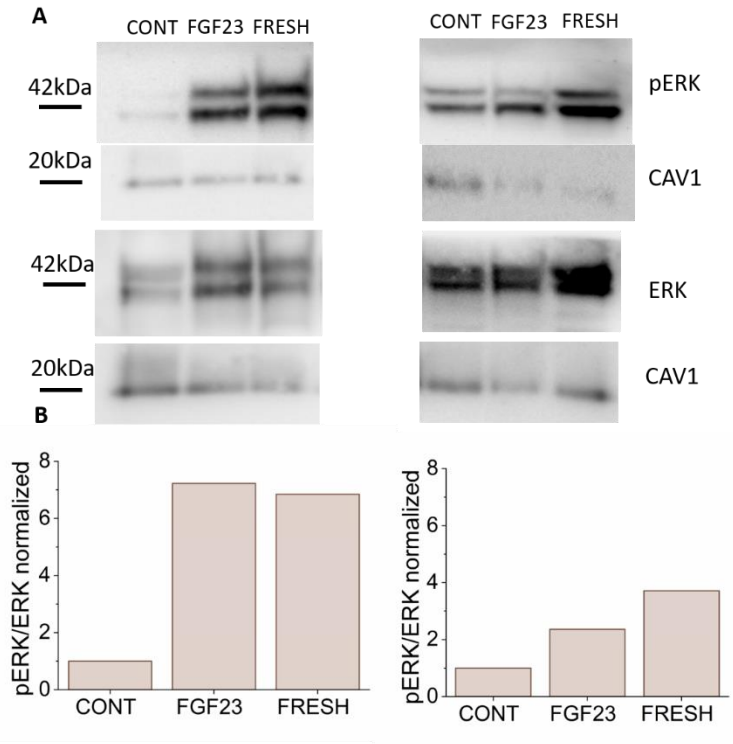

Figure 25. 48 hrs of FGF23 incubation activates the ERK pathways in SAN tissue. (A) As revealed by Western blot analysis of total protein extracts, FGF23 10 ng/mL 48hrs treatment (**FGF23**) increases levels of phosphorylated ERK in SAN cells within 48 hrs compared to incubation with vehicle (**CONT**), in **FRESH** isolated tissue ERK is highly phosphorylated. Caveolin 1 (CAV1) was used as housekeeping. **(B)** Densitometric analysis of the chemiluminescent signal, ERK and pERK were normalized on CAV1; For pERK-ERK the signal of both bands was acquired; the bar graph displayed the ratio between pERK and ERK normalized on control.

Human Induced Pluripotent Stem cells (hIPSC) derived cardiomyocytes analysis

Thanks to the collaboration with prof. A. Barbuti, we continued our experiments about the effect of FGF23 on Human Induced Pluripotent Stem Cells (hiPSC) differentiated towards the cardiac linage. This model could highlight possible actions of FGF23 on a human pacemaker cardiac cell. We started assessing the expression of FGF23 receptors and the co-receptor α-Klotho in hiPSC-derived spontaneously beating cardiomyocytes at day 15th of differentiation.

We performed reverse transcriptase PCR (RT-PCR) analyses on two different control cell line of hIPSC derived cardiomyocytes. In **Figure 26A** results of RT-PCR performed are shown. This experiment demonstrates that this cell model, at day 15th of differentiation, expresses all the FGFRs and the co-receptor α-Klotho.

We continued analysing the proteins expression of FGFR1, FGFR2 and α-Klotho by means of immunofluorescence experiments. As shown In **Figure 26B** hiPSC-derived cardiomyocytes at day 15th of differentiation express HCN4 (**Figure 26B** green), α-Klotho (**Figure 26B** red, top), FGFR1 (**Figure 26B** red, middle), FGFR2 (**Figure 26B** red, bottom) proteins.

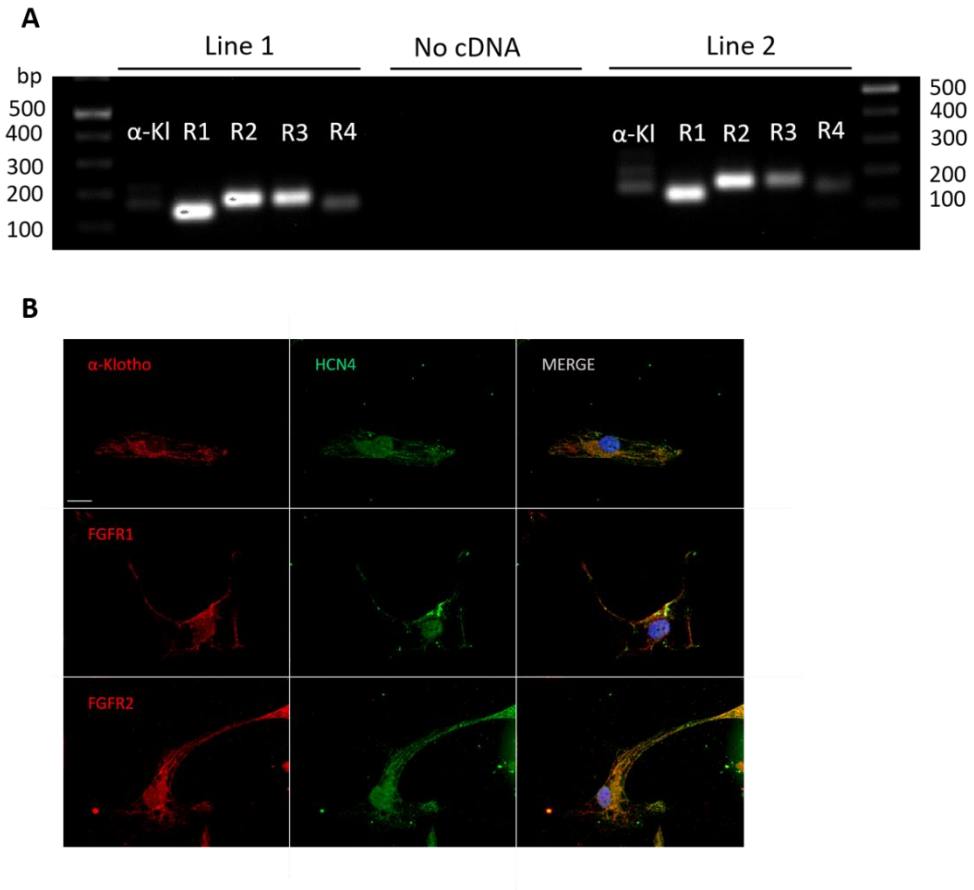

Figure 26. hiPSC-derived cardiomyocytes express FGFRs and α-Klotho. (A) RT-PCR analysis of α-Klotho and FGFR1-4 mRNAs of hiPSC-derived cardiomyocytes at day 15th of differentiation. **(B)** hiPSC-derived cardiomyocytes at day 15th of differentiation were labelled with anti-HCN4 (green), and anti-α-Klotho (red, top), anti -FGFR1 (red, middle), anti-FGFR2 (red, bottom). Nuclei were stained with DAPI (blue). Scale bar: 10μm.

Once verified the expression of FGFRs we evaluated the electrophysiological effects of FGF23 on this cell model. hiPSC-derived cardiomyocytes were incubated for 48 hrs either with FGF23 (1 ng/mL) or in control conditions. The FGF23 concentration used was 10 times lower compared to the one used in mice since in humans the FGF23 plasma levels are about 10 folds lower than in mice[40,83].

After the incubation patch-clamp recordings were performed on single spontaneously beating cells.

Representative AP traces recorded after 48 hrs incubation in control (purple) and with FGF23 1 ng/mL (orange) and mean spontaneous rate values are shown in **Figure 27A and B** respectively.

Our data highlight that FGF23 increases the hiPSC-derived cardiomyocytes AP frequency (control: 2.8±0.2 Hz; FGF23: 3.7±0.3 Hz, p<0.05).

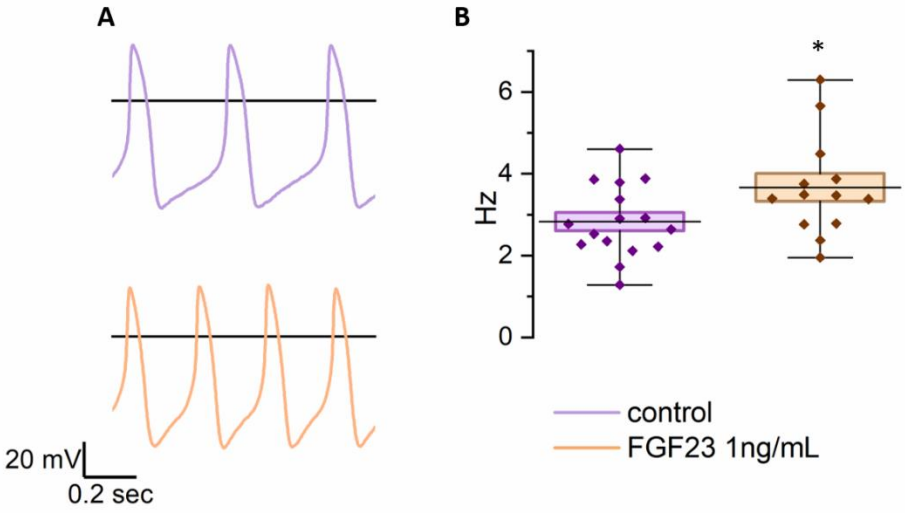

Figure 27. FGF23 increases the AP frequency of hiPSC-derived cardiomyocytes. (A) Representative AP traces recorded after 48 hrs of incubation in control (purple) and with FGF23 1 ng/ml (orange). The horizontal black line represents the value of 0 mV. **(B)** Box plot of the AP rate indicated as mean (black line) ±SEM (box): control, 2.8±0.2 Hz (n=16); FGF23 1 ng/mL 3.7±0.3 Hz (n=13). the whiskers indicate the minimum and the maximum value. *, p<0.05 vs control (Student's *t*-test).

Finally, we performed the analysis of 48 hrs of incubation with FGF23 1ng/mL on the I_f current. In Figure 28A representatives I_f current traces recorded after 48 hrs incubation in control (purple) and with FGF23 1ng/mL (orange) are reported. The g_{max}, the mean steady-state IV curves and the mean activation curves of the I_f current in the different conditions are illustrated in Figure 28B, C and D, respectively. The mean g_{max} values obtained were control, 0.052±0.005 nS/pF; FGF23 10ng/mL, 0.07±0.005 nS/pF (p<0.05).

As expected, the 48 hrs treatment with FGF23 1ng/mL increases the I_f current density in hIPSC derived spontaneously beating cardiomyocytes without altering the voltage-dependence of the channels. Furthermore, in this cell model, in agreement with data obtained in murine SAN cells, the FGF23 treatment does not affect the cells capacitance (p>0.05; Student's *t*-test, data not shown).

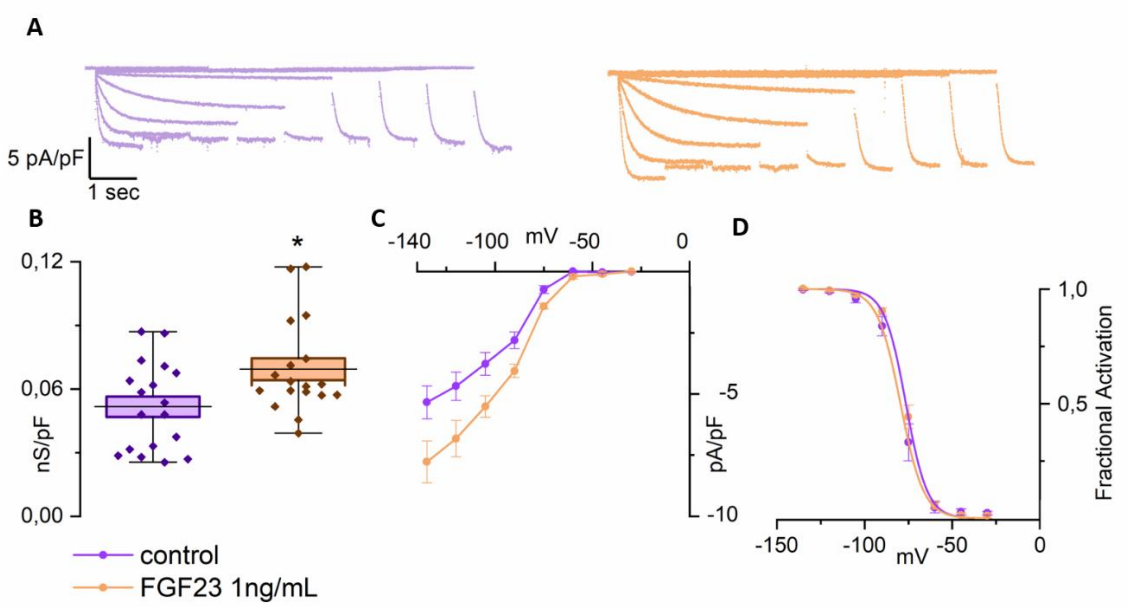

Figure 28. FGF23 increases the I_f current density of hiPSC-derived cardiomyocytes. **(A)** Representative *If* current traces recorded in control (purple) and after 48 hrs of FGF23 1 ng/mL treatment (orange). **(B)** Box plot of I_f maximal conductance (g_{max}) indicated as mean (black line) ±SEM (box): control, 0.052±0.005 nS/pF (n=16); FGF23 1ng/mL, 0.07±0.005 nS/pF (n=16); the whiskers indicate the minimum and the maximum value. **(C)** Steady-state IV and **(D)** mean I_f activation curves; mean±SEM activation $V_{1/2}$ values: control, -75.3±0.31 mV (n=10); FGF23, -76.7±0.27 mV (n=10). *, $p<0.05$ vs control (Student's *t*-test).

Discussion

FGF23 is a proteohormone manly produced by osteocytes and osteoblasts and its canonical effect is to regulate mineral metabolism through the FRS2 α/MAPK pathway activation[1]. FGF23 exerts its function mainly in the kidneys where it binds the FGFR complex which is formed by the FGFR and its co-receptor α-Klotho. It is worth pointing out that the presence α-Klotho confers to the receptor complex the specificity for FGF23[2].

In addition, FGF23 is involved in a wide number of physiological and pathological processes, in particular high circulating levels have been reported to be strongly associated with CV diseases, such as cardiac hypertrophy and arrhythmias[69]. Interestingly, several studies have shown that FGF23 modulates heart contractility[73,74,76] and is able to induce hypertrophy via activation of FGFRs alone[56,65]. Indeed, a variety of data indicate that α-Klotho is not expressed in the working myocardium[64]. Of extreme interest are the data from Takeshita and colleagues[3] indicating that the SAN tissue expresses α-Klotho and that α-Klotho KO mice display intrinsic bradycardia and easily perish for sinus arrest or sinus block as a consequence of restrain-induced stress. These pieces of evidence suggest that SAN cells, as well as tubular renal cells, are a possible physiological FGF23 target.

Our data indicate that mouse SAN cells express both membrane α-Klotho and FGFRs (mainly FGFR1; Figure 16) and, patch-clamp experiments show that FGF23 can increase the spontaneous AP frequency of these cells via an increase of the I_f current density (Figures 20 and 21). In line with the fact that FGF23 effects can be observed only after 48 hrs of incubation, and not after short or medium exposure (Figure 17, 18 and 19), we can speculate that this hormone acts by increasing f-channels synthesis or by decreasing channel degradation. This hypothesis is also supported by the increase of the $I_f g_{max}$ after FGF23 treatment.

Furthermore, the effect of FGF23 on SAN electrical activity is completely abolished in the presence of PD173074, a pan-FGFR blocker (Figures 20 and 21). This result is extremely important because it provides and additional confirmation that, in SAN cells, the effect of FGF23 is specific and mediated by the binding to the FGFR.

As reported in the literature, FGF23 preferentially binds the FGFR1/3/4[67] and, since the isoforms FGFR3/4 are poorly expressed in the SAN tissue, we can hypothesize that SAN FGF23-mediated effects result from FGFR1 activation. Our data also suggest that FGF23 requires the coreceptor α-Klotho to exert its function; indeed, when SAN tissues isolated from α-Klotho KO mice were treated with FGF23, no effect on the I_f current was observed (Figure 24). Previous works demonstrate that, if the FGFR complex includes α-Klotho, then, the binding of FGF23 triggers the activation of ERK pathway, while in the absence of α-Klotho a prevalent activation of PLCγ pathway occurs[56]. This

evidence well correlates with our western blot analysis carried out in WT mice, where an increase in the phosphorylated (active) form of ERK is observed in SAN tissues incubated with FGF23 for 48 hrs, indicating an enhanced activation of the ERK pathway (Figure 25). Taken together these data support the fact that FGF23 modulates SAN cells electrical activity by activating the receptor complex FGFR1-α-Klotho. Further experiments are necessary to better investigate the correlation existing between FGFR activation and the increased I_f current density (due to an increase synthesis or decrease degradation of f-channels). Indeed, although the activation of the receptor complex FGFR1-α-Klotho is known to mainly activate the ERK pathway, we cannot exclude a possible but minor activation of the other pathways that are known to associated with the receptor complex: the PLCγ pathway and the PI3K/AKT pathway. Previous data have shown: 1) that AKT inhibition does not affect SAN I_f[84]; 2) that PI3K inhibition induces a decrease of the I_f current and a shift of its activation curve toward mor negative potentials[85]; 3) that PLCγ activation decreases the HCN2 current and shifts its activation curve toward more positive potentials[31]; 4) a possible positive correlation between ERK activation and HCN4/ I_f current expression[86]. Since FGF23 does not induce changes in the activation curve in SAN I_f (Figure 21) we can hypothesize that the observed increase in the I_f current may be related to a still unknown ERK-dependent pathway or may be the result of a balance among the activation of the three pathways.

The data obtained in the mouse model were confirmed in hiPSC-derived spontaneously beating cardiomyocytes which express membrane α-Klotho and FGFRs (Figure 27 and 28); indeed, the incubation with FGF23 1ng/mL for 48hrs increased both the AP frequency (Figure 27) and the I_f current density (Figure 28). Since we were able to observe the same results in the two different pacemaker models (mice SAN and hiPSC-derived spontaneously beating cardiomyocytes) we can speculate that our findings should be applicable also to a human SAN.

Freshly isolated α-Klotho KO SAN cells display a decreased I_f current density compared with their WT littermates (Figure 23), and this is in agreement with the intrinsic bradycardia characterizing these mice[3]. It is important to note that the dysfunctional SAN phenotype in α-Klotho KO mice may be the results of complex effects induced by the lack of all forms of α-Klotho. Indeed, it is known that circulating α-Klotho forms can regulate several ion channels (among which hERG and KCNQ1 potassium channels that are known to be expressed in the SAN) as well as Ca^{2+} handling processes[40,41,42,43,87]. In addition, it has been reported that these mice have extremely high levels of circulating FGF23 (about 400 ng/mL)[40] that can induce additional unspecific effects. Indeed, as far as it is known, the role of α-Klotho is to increase the affinity of the receptor for FGF23, but the receptor alone (as is the case in α-Klotho KO mice) has a reduced, but still present, affinity for FGF23. Based on these assumptions and on the evidence that in KO mice the levels of FGF23 are

extremely high, the possibility of an overactivation of the receptor should also be considered. In simple terms there should be a balance between the loss of affinity (due to α-Klotho KO) and the increased receptor activation (due to the increases FGF23 concentration). Our experimental data clearly indicate that the net effect on the I_f current and on pacemaking rate is a loss of function associated with α-Klotho KO. Possible explanations for the observed decrease in I_f current density in α-Klotho KO SAN cell might be: 1) very high levels of FGF23 may be unspecific and activate different FGFRs-mediated intracellular pathways; 2) the constitutive deletion of α-Klotho might result in a remodelling of the SAN tissue; it is important to note that α-Klotho KO SAN cells display a reduced cell capacitance that might reflect a SAN remodelling (Figure 23). Further experiments are necessary to clearly identify the whole mechanism inducing SAN dysfunctions in α-Klotho KO mice, but this but such analysis would go beyond the scope of our study.

In summary, our data suggest that FGF23, via FGFR1-α-Klotho complex activation, cause an increase in I_f current conductance with a consequent rise of the AP spontaneous firing (Figure 29). The pathway linking the FGFR-α-Klotho activation and pacemaker channels modulation, as well as a possible effect of FGF23 on other SAN voltage/Ca2+-clock components, remains to be elucidated; our data only exclude a possible effect of FGF23 on *ICaL* current (Figure 22).

Whether the effect of FGF23 on the spontaneous electrical activity of SAN cells represents a homeostatic or a maladaptive response is still to be fully clarified. In literature it is well established that FGF23 contributes to ventricular hypertrophy and arrhythmias, in particular Faul and colleagues[56] revealed that in ventricular cardiomyocytes, where α-Klotho is not express, FGF23 causes hypertrophy through FGFR4-induced stimulation of the PLCγ pathway. It is also important to keep in mind that, in kidneys, which are the main functional target of FGF23, this molecule exerts its physiological action by triggering the FRS2 α/MAPK pathway in an α-Klotho dependent way[64].

In the entire body, the tissues expressing α-Klotho are very limited[39] and include the SAN[3]; in agreement with this evidence α-Klotho KO mice display intrinsic bradycardia[3]. Our data add an other piece of information since they reveal that α-Klotho KO mice show a decrease in I_f current density. Moreover, we provide evidence that FGF23 is not able to regulate the I_f current in the KO mouse model while it increases the spontaneous activity of SAN cells in the WT model.

Notably, we have observed that 48hrs SAN tissue incubation with FGF23 activates the MAPK pathway without affecting SAN cells capacitance indicating that, under these conditions, the hormone does not induce hypertrophy.

Still, the physiological significance of the FGF23 action on SAN electrical activity remains to be elucidated. It is well known that several molecules, which act as autocrine, paracrine or endocrine factors (such as thyroid and parathyroid hormones), are involved in HR regulation[27] thus suggesting a similar role for FGF23; however additional data are required to clarify this point.

Furthermore, in a recent *in-vitro* research Andrukova and co-workers[88] reported that FGF23 was able to regulate phosphate excretion in renal proximal tubules (one of its physiological targets) and the concentration used in their experiments was similar to the one employed in our experiments where we demonstrated that FGF23 modulates SAN myocytes electrical properties.

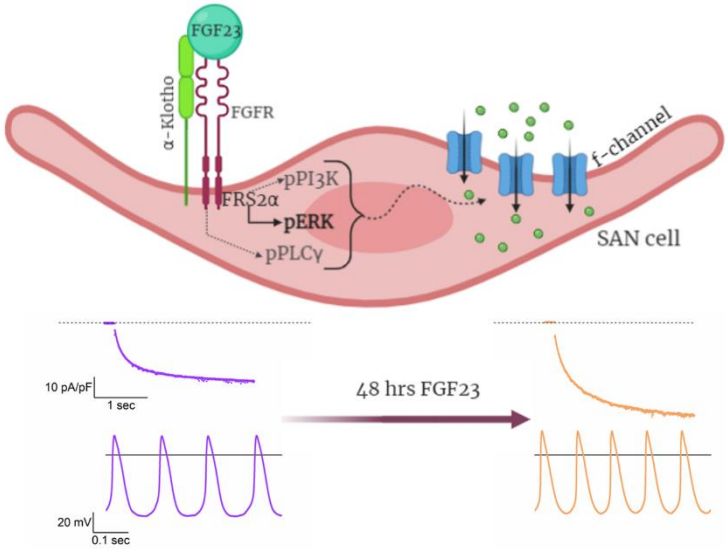

Figure 29. Schematic representation of the FGF23 effect on SAN cells. FGF23, binding to FGFR- complex cause an increase in I_f current whit a consequent rise of the AP spontaneous firing. The pathway linked to this increase in frequency may involve an unknown ERK dependent pathway or it could be a balance among the activation of all three pathways (ERK, PI3K/AKT; PLC).

One potential physiological benefit of a FGF23-mediated cardio-renal cross talk could be that the increase in AP frequency, and the consequent enhanced cardiac output, may be helpful for the increase of the renal clearance[89]. Indeed, this mechanism can contribute to regulate phosphate excretion in response to rising levels of circulating phosphate.

Although we are still far from a full understanding of the physiological significance of electrical modulation of FGF23, our data represent a first step in the characterization of this potentially new rate regulator.

Materials and Methods

Animals

All animals procedure has been accomplished in accordance with the guidelines of the care and use of laboratory animals established by Italian State (D.L. 116/1992) and European directives (86/609/CEE) and with the guidelines for ethical NIH Guide for the Care and Use of Laboratory Animals and Guidelines for Ethical Care and Welfare (2013/175) of Experimental Animals of the European Union (2010/63/EU). The procedures were approved by the Bioethical Committee of the Universidad Autónoma de Madrid, and by the General Direction of Agriculture and the Environment at the Environment Council of Madrid.

All experiments have been performed on SAN cells/cardiac tissues isolated from 2-3-month-old male WT mice (C57Bl/6J, Charles River), and 2 months-old male and female α-Klotho KO mice and their WT littermates, a transgenic strain generated by prof. Makoto Kuro-o. In the KO mice, α-Klotho gene is constitutively absent in all the tissues and only the homozygous mice display the phenotype described for the first time by prof. Makoto Kuro-o in 1997[37].

Experiments involving α-Klotho KO mice were performed in collaboration with dr. G. Ruiz-Hurtado and dr. C. Delgado Canencia, which have previously described the phenotypic characteristics of the mice strain that we used for our experiments[54]. Briefly, α-Klotho KO mice display decreased body weight and heart hypertrophy, which however, it is not associated with an increase in cells capacitance of ventricular cardiomyocytes; indeed, cardiomyocytes area was significantly smaller compared with WT littermates. Furthermore, they display impaired kidney function as revealed by the increased plasma levels of urea, blood urea nitrogen and FGF23 relative to WT littermates; in particular FGF23 plasma levels were (pg/mL) 268.3 ± 36.7 for WT mice and 457'318 ± 57'566 for KO mice[40].

Mouse SAN cells isolation

The hearts were quickly extracted and immersed in in Tyrode solution (mM: NaCl, 140; KCl, 5.4; $CaCl_2$, 1.8; $MgCl_2$, 1; D-glucose, 5.5; Hepes-NaOH, 5; pH 7.4) containing heparin (10 U/mL, Sigma-Aldrich). The SAN and the right atrium tissues were isolated. To isolate SAN myocytes we used a previously described enzymatic and mechanical standard method [90]. The enzymatic solution contained collagenase IV (224 U/mL; Worthington), elastase (1.4 U/mL; Sigma-Aldrich), and protease (0.41 U/mL; Sigma-Aldrich).

Isolated single cells were kept at 4 °C in Tyrode solution and used for the day.

SAN tissue incubation

The SAN tissues after dissection and a partial removal of atria were placed in a petri dish coated with SYLGARD 184 elastomer kit and were fixed with pins in 4 points: superior and inferior vena cava, right and left atrium (Figure 30).

SAN tissues were incubated for 48 hrs or 15 hrs with medium T1 [MEDIUM 199 (Sigma Aldrich)] complemented with Fetal Bovine Serum (FBS) 20% (GIBCO), Insulin-Transferrin-Sodium selenite (ITS) 1% (Sigma Aldrich), 2,3 ButaneDione Monoxime (BDM) 10 Mm (Sigma Aldrich) and antibiotics) at 37°C, 5% of CO2 with: vehicle [PBS 0.1% Bovine Serum Albumin (BSA-Sigma Aldrich)]; mouse FGF23 10 ng/mL (R&D systems); PD1730274 1μM (Selleckchem).

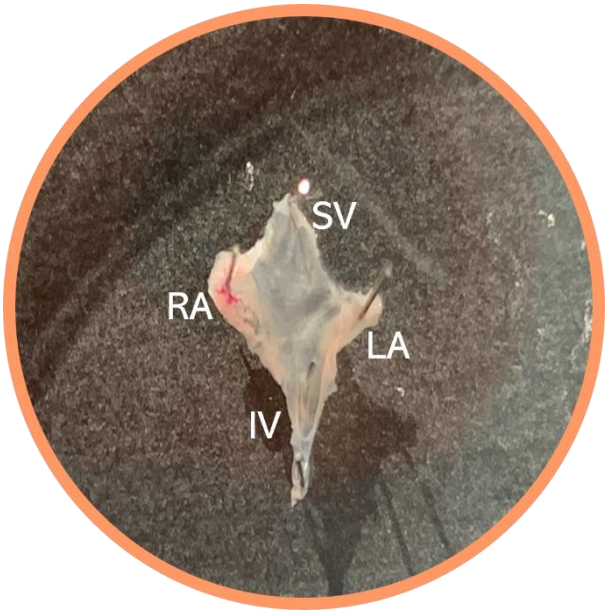

Figure 30. SAN tissue maintained in culture. The SAN tissue was placed in petri dish and fixed with pins in 4 points: SV, Superior Vena cava; IV, Inferior Vena cava; RA, Right Atrium; LA, Left Atrium.

Human induced pluripotent stem cells-derived cardiomyocytes

The human induced pluripotent stem cells (hiPSC) derived cardiomyocytes were a used in collaboration with the group of prof. A. Barbuti. The cells were obtained from healthy donors and differentiated into cardiomyocytes according to protocol reported in Benzoni et al.[91]. Two different control cell line at day 15th of differentiation were used. All the experiments were performed with the approvement of the ethical committee of the University of Milan.

Functional studies in mouse SAN cells

Single cells were isolated from the tissue as described in the previous section; the same day of cells isolation patch-clamp experiments were performed in the whole-cell configuration at 35±0.5 °C. Cells were isolated immediately after SAN dissection to perform the acute (1 minute) and 1 hr incubation experiments and after 15/48 hrs of tissue incubation to study longer exposure.
The cells were kept at 4 °C in Tyrode solution for the day of experiments, while, during the 1hr of incubation the cells were plated in 35 mm Petri dish with FGF23 10 ng/mL or vehicle (Tyrode 0.1% BSA) at room temperature in Tyrode solution.
For the acute experiments (1 min), the cells were superfused at 35±0.5 °C with FGF23 10 ng/mL or vehicle (Tyrode or modified Tyrode + 0.1% BSA).

To record action potentials cells were superfused with Tyrode solution.
A modified Tyrode solution to which $BaCl_2$ (1 mM) and $MnCl_2$ (2 mM) were added to improve I_f current dissection over other ionic components. Pipettes were filled with intracellular solution (mM): KAspartate, 130; NaCl, 10; EGTA-KOH, 5; $CaCl_2$, 2; $MgCl_2$, 2; ATP (Na-salt), 2; creatine phosphate, 5; GTP (Na-salt), 0.1; pH 7.2.
To analyze the I_{CaL} current the cells were superfused with a solution containing (mM): NMDG, 130; $CaCl_2$, 2; $MgCl_2$, 1; 4-amino-pyridine, 10; Hepes, 25; pH 7.4 and tetrodotoxin (TTX; Hellobio,10 µmol/L). Subsequently the cells were superfused with the same solution with the addition of Nifedipine 10 µmol/L, a I_{CaL} blocker; I_{CaL} was therefore measured as the Nifedipine sensible current. Pipettes were filled with intracellular solution containing (mM): CsCl, 135; $MgCl_2$, 1; ATP-(Na-salt), 4; GTP (Na-salt), 0.1; EGTA-KOH, 5; Hepes-KOH, 5; pH 7.2.

Action potentials were recorded in current-clamp configuration from single cells or small uniformly-beating aggregates as continuous traces at a sampling rate of 20 KHz and filtered at 5 KHz with pClamp software.
I_{CaL} current was recorded in single SAN myocytes (filter: 1kHz); the current-voltage (I-V) relationship and activation curve of I_{CaL} were determined by applying 150 msec depolarizing steps ranging from -60 to 50 mV (increment, 10 mV) from a holding potential (hp) of -60 mV (Figure 31A). To study inactivation a step at 0 mV (300 msec) was applied after preconditioning voltage steps (500 msec) from -70 to 20 mV and normalizing it to the maximal current (hp=-60 mV) (Figure 31B).

Activation and inactivation curves were obtained by fitting experimental points with the Boltzmann equation: y = 1/(1+exp ((V-V1/2)/s)) where V is voltage, y fractional activation, $V_{1/2}$ the half-activation/inactivation voltage, and s the inverse-slope factor.
The current density was obtained normalizing the peak current amplitude to the cell capacitance.

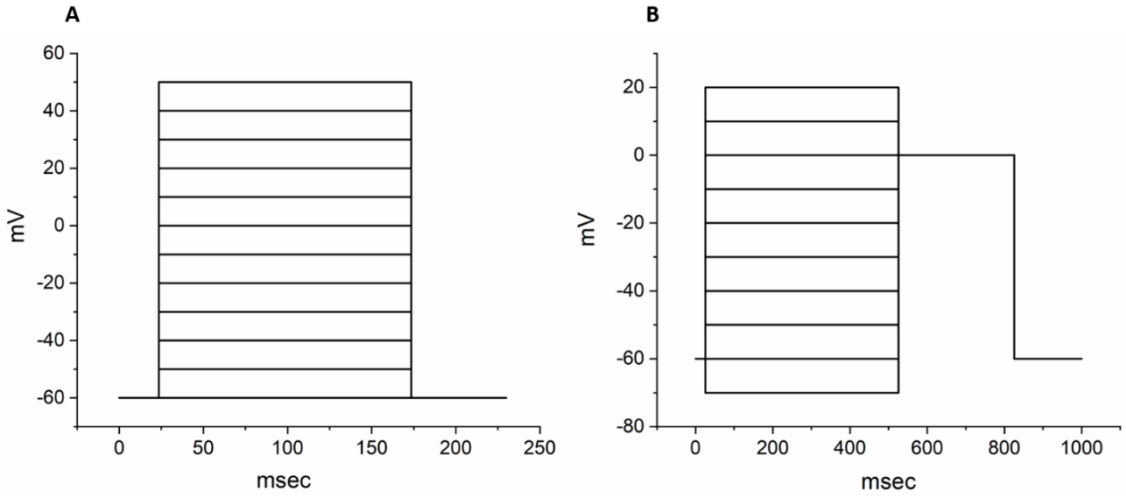

Figure 31. I_{CaL} current voltage steps protocols. (A) Protocol used to investigate the current-voltage (I-V) relationship and activation of *ICaL* current. (B) Protocol used to analyse the inactivation of *ICaL* current.

I_f current was recorded from single SAN myocytes (filter: 1 kHz) by means of different protocols deepening on the nature of the experiment.
To test the acute effect of FGF23, double step protocol which consisted of a 1.5 sec pulse to -75 mV (close to the V1/2 of the activation curve), followed by a 500 msec voltage pulse to -125 mV was used (hp=-35mV).
For the experiments on C57Bl/6J mice the current-voltage (I-V) relationship and activation curve of the I_f current were obtained by applying a step protocol (hp=-30mV) with a first step to a test voltage in the range −30/−135 mV (increment 15 mV), a second step to −125 mV and a third step to 10 mV. Test step durations varied from 10 sec at −30mV to 5.1sec at −135mV to allow full current activation at each voltage (Figure 32A). The current density was obtained normalizing the test step current amplitude to the cell capacitance. The activation curve was acquired from a second step currents measured at −125 mV, after normalization to maximum amplitude. the data points were fitted with the Boltzmann distribution, described above, to obtain the activation variable.
The g_{max} was obtained as the slope of the linear fit of the fully activated currents (-120 and -135 mV).

For the kl/kl mice experiments the I-V relationship and activation curve of the I_f current were obtained by applying a two-step protocol (hp=-30mV) with a first step to a test voltage in the range −30/−135 mV (increment 15 or 30 mV) and a second step to +10 mV. Test step durations varied from 10 sec at −30mV to 5.1 sec at −135mV to allow full current activation at each voltage (Figure 32B). The current density was obtained normalizing the test step current amplitude to the cell capacitance. The activation curve was acquired from the tail current recorded at +10 mV after normalization to maximum amplitude. the data points were fitted with the Boltzmann distribution.

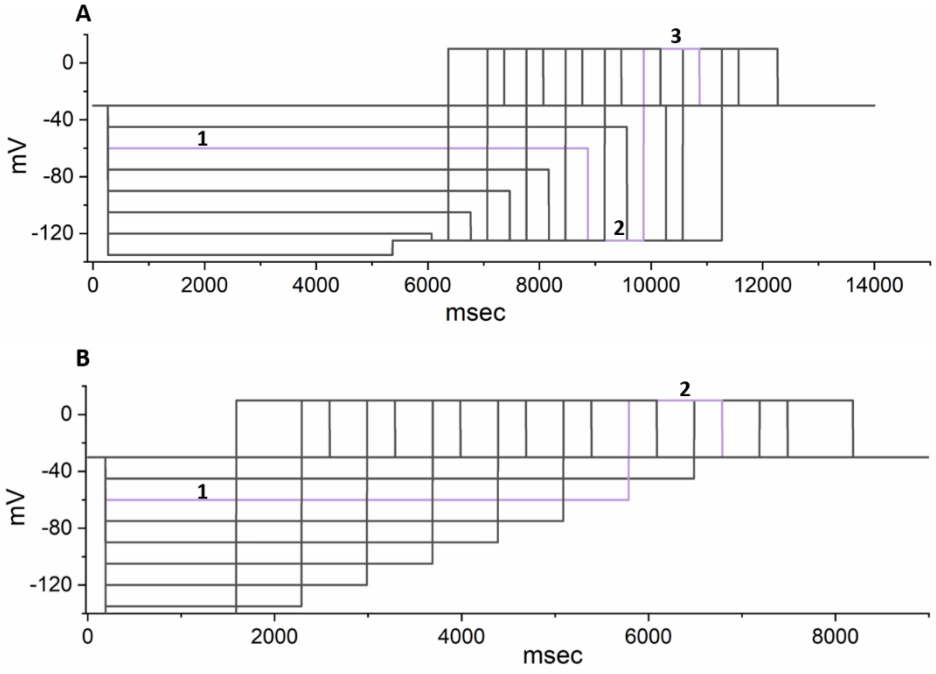

Figure 32. I_f current voltage steps protocols. (A) Protocol used to investigate the I-V relationship and activation of the *If* current in C57Bl/6J WT mice. (B) Protocol used to analyse the I-V relationship and activation of the *If* current in α-Klotho KO mice. In purple one sweep example in which the different steps are highlighted.

Functional studies (hiPSC) derived cardiomyocytes

hiPSC-derived cardiomyocytes were incubated for 48 hrs at 37°C and 5% of CO2 with either vehicle (PBS 0.1% BSA) or human FGF23 1 ng/mL (Sigma-Aldrich).

After the incubation whole cells patch-clamp recordings were performed at 36±1°C.

Pipettes were filled with intracellular solution (mM): KCl, 120; Hepes-NaOH, 20; EGTA-KOH, 0.1; $MgCl_2$, 2; ATP (Mg-salt), 10; pH 7.1.

To record APs the cells were perfused with Tyrode high glucose solution (pH 7.4) containing (mM): NaCl, 137; KCl, 5; $CaCl_2$, 2; $MgCl_2$, 1; D-glucose, 10; Hepes-NaOH, 10; pH 7.4

To dissect I_f current $BaCl_2$ (1 mM) and $MnCl_2$ (2 mM) were added to the solution.

The AP and I_f recording and analyses were performed as described in the previous section. Precisely , for the I_f current the I-V relationship and activation curve of the were obtained by applying a step protocol (hp=-30mV) with a first step to a test voltage in the range −30/−135 mV (increment 15 mV), a second step to −125 mV and a third step to 10 mV. Test step durations varied from 8 sec at −30mV to 1.7 sec at −135mV to allow full current activation at each voltage (Figure 33).
The activation curve was acquired from a second step currents measured at −125 mV, after normalization to maximum amplitude.
The g_{max} was obtained as the slope of the linear fit of the fully activated currents (-120 and -135 mV) acquired with I-V protocols.

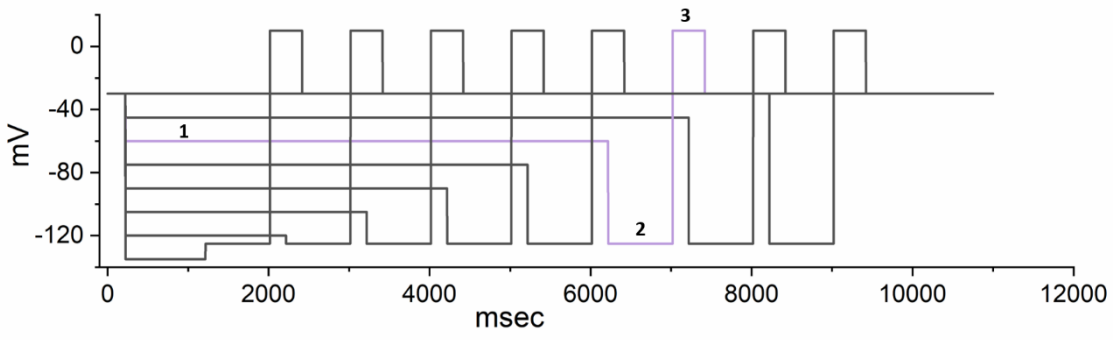

Figure 33. I_f current voltage steps protocol. Protocol used to investigate the I-V relationship and activation of the *If* current in hIPSC-derived cardiomyocytes. In purple one sweep example in which the different steps are highlighted.

Reverse transcriptase PCR (RT-PCR) analysis

The mRNA form hiPSC derived cardiomyocytes was extract with Direct-zol RNA mini prep KIT (ZYMO RESEARCH) and reverse transcribed using Maxima First Strand cDNA Synthesis KIT (Thermo Fisher Scientific). RT-PCR was performed using 40 ng of cDNA with PCR master mix FastStart Taq Polymerase (ROCHE). Primers used for RT-PCR are listed in Table 1.

Reverse transcriptase (RT) quantitative PCR (qPCR) analysis

The tissues were snap frozen after the isolation from the heart of WT mice. 2 or 3 SAN tissues or right atria were used for each sample, total mRNA was isolated using TRIzol reagent (Thermo Fisher Scientific). After the extraction 1 µg of mRNA was reverse transcribed using a commercial KIT (Maxima First Strand cDNA Synthesis; Thermo Fisher Scientific). qPCR was performed in triplicate using 20 ng of cDNA with Maxima SYBR Green qPCR Master Mix (Thermo Fisher Scientific) and specific

primers in a Real-Time PCR detection system (gene 9600 Plus, BIOER). All primer pairs had efficiency > 95%.

Expression data were analysed using 2^(-ΔCT) method relative to expression level of housekeeping gene α-actinin or 18S. Primers used for qPCR were listed in Table 1. Primers used for α-Klotho detect the membrane form only.

Gene	RTqPCR (mouse)	RT-PCR (human)
α-Klotho	F_ ACGTTCAAGTGGACACTACTCT	F_TCAGCCCCTAGAAGGGACAT
	R _GGTTATCTGAGGCCGGATGG	R_CTTGGTCACAACCCCATCCA
FGFR1	F_ ACTCTGCATGGTTGACCGTT	R_TTGTAGACGATGACCGACCC
	R _AGGTAGAGCGGTGAGGTCAT	R_TTGTAGACGATGACCGACCC
FGFR2	F_TGTGGTCCCGTCAGACAAAG	F_TGGAAAGTGTGGTCCCATCTG
	R_TGGGCATCGCTGTAAACCTT	R_ACTCTACGTCTCCTCCGACC
FGFR3	F_ CTACTTCCGAGCCTCCTGGT	F_CTCCTCGGAGTCCTTGGGGA
	R _CATCCTTAGCCCAGACCGTG	R_GCCATCCTTGACCCAGACAG
FGFR4	F_ ATCAGGCTCACTGGTTCTGC	F_ATCCTGTACGCGTCGGGCTC
	R _TCCAAAGAGAACTGTCGGGC	R_CTCCAGGGAGAACTGTCGGG

Table 1. Primer list. In the left column the primer used for the RTqPCR, in the right for the RT-PCR; Forward (F) and Reverse (R). For the RT-PCR the expected lengths of the bands are (bp): 163 αKlotho, 139 FGFR1, 174 FGFR2, 175 FGFR3, 153 FGFR4.

Immunofluorescence analysis

Immunofluorescence were performed in the same way on both hiPSC-derived cardiomyocytes and single murine SAN cells. The cells were fixed with 4 % paraformaldehyde in phosphate buffered saline (PBS) for 8 minutes at room temperature and treated with PBS containing Triton X-100 0.3% Sigma Aldrich); $MgCl_2$, 3 mM; donkey serum 10% (Abcam) to permeabilize the membrane and blocking non-specific binding. The cells were then incubated with the primary antibodies diluted in PBS containing BSA 1%; donkey serum 2% at 4°C overnight. Primary antibodies used were reported below. After washing with PBS, the cells were incubated one hour at room temperature with an Alexa fluor 594 donkey anti-rabbit antibody (Invitrongen) and an Alexa flour 488 donkey anti-rat antibody (Invitrongen). Nuclei were stained with 0,5 µg/ml DAPI (4',6-diamidino-2- phenylindole). The samples were acquired using a Video Confocal fluorescence microscope equipped with an 40x or 60x oil objective. The Video Confocal settings were maintained constant in all the experiments when the same antibody was used. For each immunofluorescence experiment the images were background subtracted using settings that allow us to have absence of staining when

the primary antibody was omitted (secondary antibodies only; Figure 30A). Furthermore, to test the Klotho primary antibody specificity we performed immunofluorescence analysis on PC12 undifferentiated cells, that do not express α-Klotho protein[67] (Figure 30B). The specificity of antibodies used for the detection of FGFR1[92] and FGFR2[93] were already reported in literature.

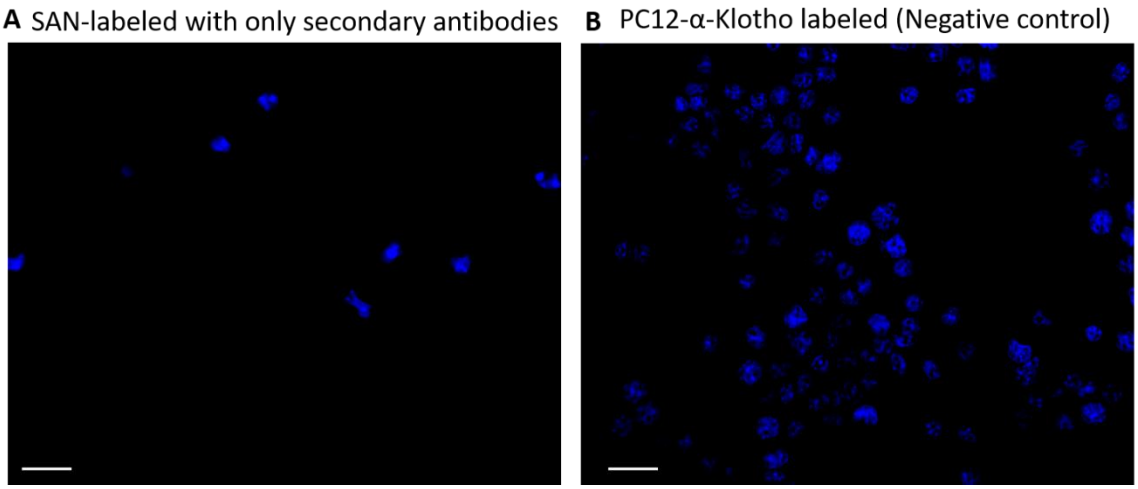

Figure 30. Immunofluorescence negative controls. (A) SAN cells labeled only with the secondary antibodies Alexa fluor 594 donkey anti-rabbit and an Alexa flour 488 donkey anti-rat. **(B)** PC12 undifferentiated cells labeled with anti α-Klotho primary antibody and Alexa fluor 594 donkey anti-rabbit secondary antibody. The images have been acquired with the same settings used for the positive cells labeled (Figure 16B). Nuclei are stained with DAPI (Blue). Scale bar 20 μM.

Western blotting analysis

The tissues were snap frozen after the isolation from the heart. Total protein extracts were prepared from 3 or 4 SAN for each sample. Tissues were lysate in 500 μL of RIPA buffer (Sigma-Aldrich), supplemented with protease inhibitor cocktail (Sigma-Aldrich) and phosphatase inhibitor cocktail set V (Millipore), using T10 basic ULTRA-TURRAX® homogenizer (IKA); afterward the lysate was passed through an insulin needle 10 times and sonicated 5 times for 30 seconds; finally it was incubated for about 1 hour at 4°C under constant agitation. The extract was centrifuged at 2000 RCF for 20 min at 4°C and the supernatant was quantified by means of a BCA assay (Life Technology).

When the samples were too dilute, they were overnight precipitated in 80% Acetone ≥99.5% (Sigma-Aldrich) and later the precipitated pellets were resuspended in appropriated volume of RIPA buffer (Sigma-Aldrich).

For western blot, the protein extracts were heated at 99°C for 5 minutes in SDS-PAGE solubilizing buffer (58 mM Tris HCl, 10% glycerol, 2% SDS, 0.004% bromophenol blue, pH 6.8) containing 2.5%

β-mercaptoethanol. Equal amounts of protein (30 µg) were loaded onto a 4-12% SDS-polyacrylamide gel (Thermo Fisher Scientific) which were run at 100 V for 1/2 hrs and transferred overnight at 30 V to a PVDF membrane using an iBLOT system (Biorad).
the membrane was blocked in TBST (Tris HCl ,20 mM; NaCl, 150 mM; pH 7.5, Tween 20, 0.1%) with 5% milk powder (Blotting Grade Blocker Non-Fat Dry Milk; Biorad) or BSA (Sigma Aldrich) and afterwards it was incubated with primary antibody reported below at 4°C overnight.
Following several washes with TBST the membrane was incubated 1hr at room temperature with the appropriate secondary horseradish peroxidase (HRP)-linked secondary antibodies (Jackson ImmunoReseaech).
For chemiluminescent acquisition Chemidoc system (BioRAD) was used after membrane incubation with SuperSignal™ West Pico or Femto PLUS Chemiluminescent Substrate (Thermo Fisher Scientific).
The phosphorylated and the total proteins were detected on the same lane membrane before and after stripping procedure respectively. the membrane was stripped of the phosphorylated antibodies by incubating it 2 times for 15 minutes in stripping buffer (Glycine, 5mM; SDS, 0.1%; Tween 20, 1%; pH 2.2) at room temperature. After stripping procedure, the absence of signal was verified, and the protocol was restarted from the blocking process.
The bands were densitometrically analysed using the ImageJ software.

Primary Antibodies

For immunofluorescence analysis the following primary antibodies were used:
-Rabbit anti-Klotho (SAB3500604, Sigma-Aldrich) 1:100;
-Rabbit anti-FGF Receptor 1 (D8E4 XP, Cell signalling technology) 1:50;
-Rabbit anti-FGF Receptor 2 (Ab10648, Abcam) 1:100;
-Rat anti-HCN4 (MA3-903, Thermo Fisher Scientific) 1:100.

For western blotting analysis the subsequent primary antibodies were used:
-Rabbit anti-p44/42 MAPK Erk1/2 (#4695, cell signaling technology) 1:5000;
-Rabbit anti-phospho p44/42 MAPK Erk1/2 (#4370, cell signaling technology) 1:1500;
-Rabbit anti Caveloin1 (Ab2910, Abcam) 1:1000

Statistical Analysis

Statistical differences were determined at the $p<0.05$ level by Student's *t*-test or one-way ANOVA followed by Fisher test. All values are given as mean±SEM

Supplementary Materials

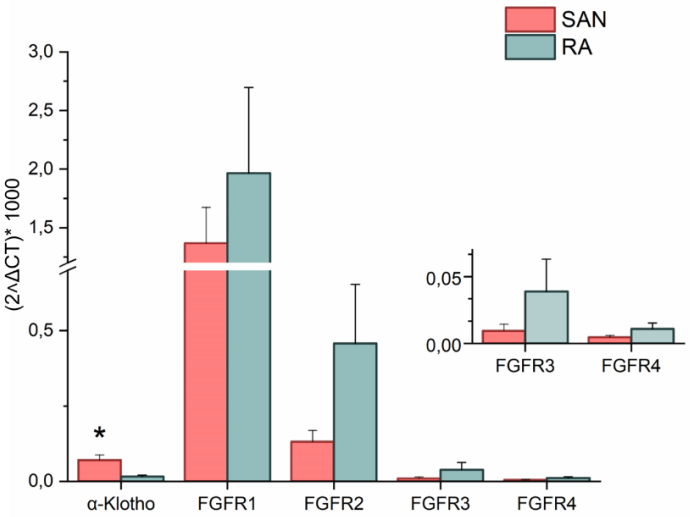

Figure S1. α-Klotho and FGFR1-4 mRNAs normalized with α-actinin. RT-qPCR analysis of α-Klotho and FGFR1-4 mRNAs in SAN and right atrium tissues normalized with α-actinin (n=4/5). The insert shows FGFR3 and FGFR4 expression data in an expanded scale. *, p<0.05 *vs* Right Atrium (Student's *t*-test).

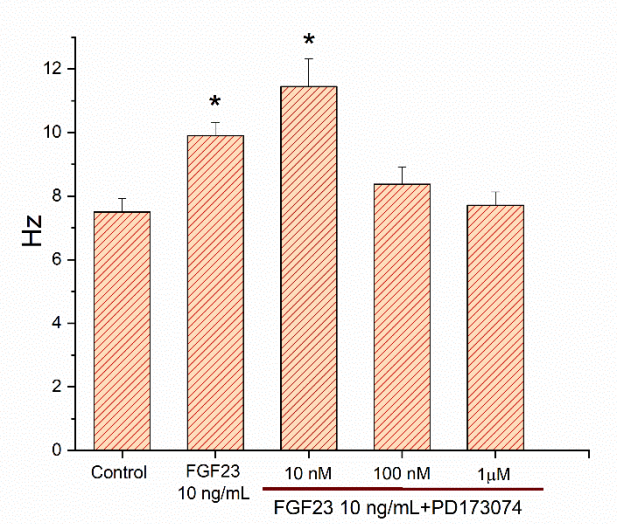

Figure S2. PD173074 100nM and1μM concentrations are required to abolish the FGF23-induced increase of SAN APs frequency. Bar graphs of the APs rate indicated as mean±SEM: control, 7.5±0.4 Hz (n=16); FGF23, 9.9±0.4 Hz (n=16); FGF23+PD173074 10nM 11,4±0.9 Hz (n=6); FGF23+PD173074 100 nM 8.5±0.4 Hz (n=23); FGF23+PD173074 1μM 7.9±0.3 Hz (n=8). *, p<0.05 vs control treated cells (One Way ANOVA, followed by Fisher test).

Bibliography

1 Erben, R. G. & Andrukhova, O. FGF23-Klotho signaling axis in the kidney. *Bone* 100, 62-68, doi:10.1016/j.bone.2016.09.010 (2017).

2 Erben, R. G. Physiological Actions of Fibroblast Growth Factor-23. *Front Endocrinol (Lausanne)* 9, 267, doi:10.3389/fendo.2018.00267 (2018).

3 Takeshita, K. *et al.* Sinoatrial node dysfunction and early unexpected death of mice with a defect of klotho gene expression. *Circulation* 109, 1776-1782, doi:10.1161/01.CIR.0000124224.48962.32 (2004).

4 Chen, Y. J., Chen, Y. C., Yeh, H. I., Lin, C. I. & Chen, S. A. Electrophysiology and arrhythmogenic activity of single cardiomyocytes from canine superior vena cava. *Circulation* 105, 2679-2685, doi:10.1161/01.cir.0000016822.96362.26 (2002).

5 Cheng, H., Smith, G. L., Hancox, J. C. & Orchard, C. H. Inhibition of spontaneous activity of rabbit atrioventricular node cells by KB-R7943 and inhibitors of sarcoplasmic reticulum Ca(2+) ATPase. *Cell Calcium* 49, 56-65, doi:10.1016/j.ceca.2010.11.008 (2011).

6 Wongcharoen, W. *et al.* Effects of a Na+/Ca2+ exchanger inhibitor on pulmonary vein electrical activity and ouabain-induced arrhythmogenicity. *Cardiovasc Res* 70, 497-508, doi:10.1016/j.cardiores.2006.02.026 (2006).

7 Dobrzynski, H. *et al.* Structure, function and clinical relevance of the cardiac conduction system, including the atrioventricular ring and outflow tract tissues. *Pharmacol Ther* 139, 260-288, doi:10.1016/j.pharmthera.2013.04.010 (2013).

8 Lei, M., Brown, H. F. & Terrar, D. A. Modulation of delayed rectifier potassium current, iK, by isoprenaline in rabbit isolated pacemaker cells. *Exp Physiol* 85, 27-35 (2000).

9 DiFrancesco, D., Ferroni, A., Mazzanti, M. & Tromba, C. Properties of the hyperpolarizing-activated current (if) in cells isolated from the rabbit sino-atrial node. *J Physiol* 377, 61-88, doi:10.1113/jphysiol.1986.sp016177 (1986).

10 Mangoni, M. E. *et al.* Functional role of L-type Cav1.3 Ca2+ channels in cardiac pacemaker activity. *Proc Natl Acad Sci U S A* 100, 5543-5548, doi:10.1073/pnas.0935295100 (2003).

11 Lakatta, E. G., Maltsev, V. A. & Vinogradova, T. M. A coupled SYSTEM of intracellular Ca2+ clocks and surface membrane voltage clocks controls the timekeeping mechanism of the heart's pacemaker. *Circ Res* 106, 659-673, doi:10.1161/CIRCRESAHA.109.206078 (2010).

12 Torrente, A. G. *et al.* L-type Cav1.3 channels regulate ryanodine receptor-dependent Ca2+ release during sino-atrial node pacemaker activity. *Cardiovasc Res* 109, 451-461, doi:10.1093/cvr/cvw006 (2016).

13 Mangoni, M. E. & Nargeot, J. Genesis and regulation of the heart automaticity. *Physiol Rev* 88, 919-982, doi:10.1152/physrev.00018.2007 (2008).

14 Lakatta, E. G., Vinogradova, T. M. & Maltsev, V. A. The missing link in the mystery of normal automaticity of cardiac pacemaker cells. *Ann N Y Acad Sci* 1123, 41-57, doi:10.1196/annals.1420.006 (2008).

15 DiFrancesco, D. A study of the ionic nature of the pace-maker current in calf Purkinje fibres. *J Physiol* 314, 377-393, doi:10.1113/jphysiol.1981.sp013714 (1981).

16 DiFrancesco, D. & Tortora, P. Direct activation of cardiac pacemaker channels by intracellular cyclic AMP. *Nature* 351, 145-147, doi:10.1038/351145a0 (1991).

17 Accili, E. A., Proenza, C., Baruscotti, M. & DiFrancesco, D. From funny current to HCN channels: 20 years of excitation. *News Physiol Sci* 17, 32-37, doi:10.1152/physiologyonline.2002.17.1.32 (2002).

18 Zagotta, W. N. *et al.* Structural basis for modulation and agonist specificity of HCN pacemaker channels. *Nature* 425, 200-205, doi:10.1038/nature01922 (2003).

19 Clapham, D. E. Not so funny anymore: pacing channels are cloned. *Neuron* 21, 5-7, doi:10.1016/s0896-6273(00)80508-5 (1998).

20 Viscomi, C. *et al.* C terminus-mediated control of voltage and cAMP gating of hyperpolarization-activated cyclic nucleotide-gated channels. *J Biol Chem* 276, 29930-29934, doi:10.1074/jbc.M103971200 (2001).

21 Altomare, C. *et al.* Integrated allosteric model of voltage gating of HCN channels. *J Gen Physiol* 117, 519-532, doi:10.1085/jgp.117.6.519 (2001).

22 Stieber, J., Stockl, G., Herrmann, S., Hassfurth, B. & Hofmann, F. Functional expression of the human HCN3 channel. *J Biol Chem* 280, 34635-34643, doi:10.1074/jbc.M502508200 (2005).

23 Postea, O. & Biel, M. Exploring HCN channels as novel drug targets. *Nat Rev Drug Discov* 10, 903-914, doi:10.1038/nrd3576 (2011).

24 Mangoni, M. E. *et al.* Bradycardia and slowing of the atrioventricular conduction in mice lacking CaV3.1/alpha1G T-type calcium channels. *Circ Res* 98, 1422-1430, doi:10.1161/01.RES.0000225862.14314.49 (2006).

25 Zamponi, G. W., Striessnig, J., Koschak, A. & Dolphin, A. C. The Physiology, Pathology, and Pharmacology of Voltage-Gated Calcium Channels and Their Future Therapeutic Potential. *Pharmacol Rev* 67, 821-870, doi:10.1124/pr.114.009654 (2015).

26 Catterall, W. A. Voltage-gated calcium channels. *Cold Spring Harb Perspect Biol* 3, a003947, doi:10.1101/cshperspect.a003947 (2011).

27 MacDonald, E. A., Rose, R. A. & Quinn, T. A. Neurohumoral Control of Sinoatrial Node Activity and Heart Rate: Insight From Experimental Models and Findings From Humans. *Front Physiol* 11, 170, doi:10.3389/fphys.2020.00170 (2020).

28 Kaumann, A. J. & Molenaar, P. Modulation of human cardiac function through 4 beta-adrenoceptor populations. *Naunyn Schmiedebergs Arch Pharmacol* 355, 667-681, doi:10.1007/pl00004999 (1997).

29 Hara, M. *et al.* Positive chronotropic actions of parathyroid hormone and parathyroid hormone-related peptide are associated with increases in the current, I(f), and the slope of the pacemaker potential. *Circulation* 96, 3704-3709, doi:10.1161/01.cir.96.10.3704 (1997).

30 Sugimoto, T. *et al.* Interrelationship between haemodynamic state and serum intact parathyroid hormone levels in patients with chronic heart failure. *Heart* 99, 111-115, doi:10.1136/heartjnl-2012-302779 (2013).

31 Pian, P., Bucchi, A., Decostanzo, A., Robinson, R. B. & Siegelbaum, S. A. Modulation of cyclic nucleotide-regulated HCN channels by PIP(2) and receptors coupled to phospholipase C. *Pflugers Arch* 455, 125-145, doi:10.1007/s00424-007-0295-2 (2007).

32 Harmer, N. J., Pellegrini, L., Chirgadze, D., Fernandez-Recio, J. & Blundell, T. L. The crystal structure of fibroblast growth factor (FGF) 19 reveals novel features of the FGF family and offers a structural basis for its unusual receptor affinity. *Biochemistry* 43, 629-640, doi:10.1021/bi035320k (2004).

33 Martin, A., David, V. & Quarles, L. D. Regulation and function of the FGF23/klotho endocrine pathways. *Physiol Rev* 92, 131-155, doi:10.1152/physrev.00002.2011 (2012).

34 Ornitz, D. M. & Itoh, N. The Fibroblast Growth Factor signaling pathway. *Wiley Interdiscip Rev Dev Biol* 4, 215-266, doi:10.1002/wdev.176 (2015).

35 Dai, S., Zhou, Z., Chen, Z., Xu, G. & Chen, Y. Fibroblast Growth Factor Receptors (FGFRs): Structures and Small Molecule Inhibitors. *Cells* 8, doi:10.3390/cells8060614 (2019).

36 Hughes, S. E. Differential expression of the fibroblast growth factor receptor (FGFR) multigene family in normal human adult tissues. *J Histochem Cytochem* 45, 1005-1019, doi:10.1177/002215549704500710 (1997).

37 Kuro-o, M. *et al.* Mutation of the mouse klotho gene leads to a syndrome resembling ageing. *Nature* 390, 45-51, doi:10.1038/36285 (1997).

38 Xu, Y. & Sun, Z. Molecular basis of Klotho: from gene to function in aging. *Endocr Rev* 36, 174-193, doi:10.1210/er.2013-1079 (2015).

39 Lim, K. *et al.* alpha-Klotho Expression in Human Tissues. *J Clin Endocrinol Metab* 100, E1308-1318, doi:10.1210/jc.2015-1800 (2015).

40 Navarro-Garcia, J. A. *et al.* Enhanced Klotho availability protects against cardiac dysfunction induced by uraemic cardiomyopathy by regulating Ca(2+) handling. *Br J Pharmacol* 177, 4701-4719, doi:10.1111/bph.15235 (2020).

41 Huang, C. L. Regulation of ion channels by secreted Klotho: mechanisms and implications. *Kidney Int* 77, 855-860, doi:10.1038/ki.2010.73 (2010).

42 Munoz, C. *et al.* Klotho sensitivity of the hERG channel. *FEBS Lett* 587, 1663-1668, doi:10.1016/j.febslet.2013.04.011 (2013).

43 Almilaji, A. *et al.* Upregulation of KCNQ1/KCNE1 K+ channels by Klotho. *Channels (Austin)* 8, 222-229, doi:10.4161/chan.27662 (2014).

44 Bonewald, L. F. & Wacker, M. J. FGF23 production by osteocytes. *Pediatr Nephrol* 28, 563-568, doi:10.1007/s00467-012-2309-3 (2013).

45 Andrukhova, O. *et al.* FGF23 regulates renal sodium handling and blood pressure. *EMBO Mol Med* 6, 744-759, doi:10.1002/emmm.201303716 (2014).

46 Andrukhova, O. *et al.* FGF23 promotes renal calcium reabsorption through the TRPV5 channel. *EMBO J* 33, 229-246, doi:10.1002/embj.201284188 (2014).

47 Masuyama, R. *et al.* Vitamin D receptor in chondrocytes promotes osteoclastogenesis and regulates FGF23 production in osteoblasts. *J Clin Invest* 116, 3150-3159, doi:10.1172/JCI29463 (2006).

48 Lavi-Moshayoff, V., Wasserman, G., Meir, T., Silver, J. & Naveh-Many, T. PTH increases FGF23 gene expression and mediates the high-FGF23 levels of experimental kidney failure: a bone parathyroid feedback loop. *Am J Physiol Renal Physiol* 299, F882-889, doi:10.1152/ajprenal.00360.2010 (2010).

49 Glosse, P. *et al.* AMP-activated kinase is a regulator of fibroblast growth factor 23 production. *Kidney Int* 94, 491-501, doi:10.1016/j.kint.2018.03.006 (2018).

50 David, V. *et al.* Inflammation and functional iron deficiency regulate fibroblast growth factor 23 production. *Kidney Int* 89, 135-146, doi:10.1038/ki.2015.290 (2016).

51 Shimada, T. *et al.* Vitamin D receptor-independent FGF23 actions in regulating phosphate and vitamin D metabolism. *Am J Physiol Renal Physiol* 289, F1088-1095, doi:10.1152/ajprenal.00474.2004 (2005).

52 Meir, T. *et al.* Parathyroid hormone activates the orphan nuclear receptor Nurr1 to induce FGF23 transcription. *Kidney Int* 86, 1106-1115, doi:10.1038/ki.2014.215 (2014).

53 Kurosu, H. *et al.* Suppression of aging in mice by the hormone Klotho. *Science* 309, 1829-1833, doi:10.1126/science.1112766 (2005).

54 Kuro-o, M. Klotho and aging. *Biochim Biophys Acta* 1790, 1049-1058, doi:10.1016/j.bbagen.2009.02.005 (2009).

55 Kuro, O. M. Molecular Mechanisms Underlying Accelerated Aging by Defects in the FGF23-Klotho System. *Int J Nephrol* 2018, 9679841, doi:10.1155/2018/9679841 (2018).

56 Faul, C. *et al.* FGF23 induces left ventricular hypertrophy. *J Clin Invest* 121, 4393-4408, doi:10.1172/JCI46122 (2011).

57 Shimada, T. *et al.* Targeted ablation of Fgf23 demonstrates an essential physiological role of FGF23 in phosphate and vitamin D metabolism. *J Clin Invest* 113, 561-568, doi:10.1172/JCI19081 (2004).

58 Yuan, Q. *et al.* FGF-23/Klotho signaling is not essential for the phosphaturic and anabolic functions of PTH. *J Bone Miner Res* 26, 2026-2035, doi:10.1002/jbmr.433 (2011).

59 Hesse, M., Frohlich, L. F., Zeitz, U., Lanske, B. & Erben, R. G. Ablation of vitamin D signaling rescues bone, mineral, and glucose homeostasis in Fgf-23 deficient mice. *Matrix Biol* 26, 75-84, doi:10.1016/j.matbio.2006.10.003 (2007).

60 Ichikawa, S. *et al.* A homozygous missense mutation in human KLOTHO causes severe tumoral calcinosis. *J Clin Invest* 117, 2684-2691, doi:10.1172/JCI31330 (2007).

61 Brownstein, C. A. *et al.* A translocation causing increased alpha-klotho level results in hypophosphatemic rickets and hyperparathyroidism. *Proc Natl Acad Sci U S A* 105, 3455-3460, doi:10.1073/pnas.0712361105 (2008).

62 John, G. B., Cheng, C. Y. & Kuro-o, M. Role of Klotho in aging, phosphate metabolism, and CKD. *Am J Kidney Dis* 58, 127-134, doi:10.1053/j.ajkd.2010.12.027 (2011).

63 Mohammadi, M. *et al.* A tyrosine-phosphorylated carboxy-terminal peptide of the fibroblast growth factor receptor (Flg) is a binding site for the SH2 domain of phospholipase C-gamma 1. *Mol Cell Biol* 11, 5068-5078, doi:10.1128/mcb.11.10.5068 (1991).

64 Richter, B. & Faul, C. FGF23 Actions on Target Tissues-With and Without Klotho. *Front Endocrinol (Lausanne)* 9, 189, doi:10.3389/fendo.2018.00189 (2018).

65 Grabner, A. *et al.* Activation of Cardiac Fibroblast Growth Factor Receptor 4 Causes Left Ventricular Hypertrophy. *Cell Metab* 22, 1020-1032, doi:10.1016/j.cmet.2015.09.002 (2015).

66 Tucker Zhou, T. B., King, G. D., Chen, C. & Abraham, C. R. Biochemical and functional characterization of the klotho-VS polymorphism implicated in aging and disease risk. *J Biol Chem* 288, 36302-36311, doi:10.1074/jbc.M113.490052 (2013).

67 Kurosu, H. *et al.* Regulation of fibroblast growth factor-23 signaling by klotho. *J Biol Chem* 281, 6120-6123, doi:10.1074/jbc.C500457200 (2006).

68 Chen, G. *et al.* alpha-Klotho is a non-enzymatic molecular scaffold for FGF23 hormone signalling. *Nature* 553, 461-466, doi:10.1038/nature25451 (2018).

69 Itoh, N. & Ohta, H. Pathophysiological roles of FGF signaling in the heart. *Front Physiol* 4, 247, doi:10.3389/fphys.2013.00247 (2013).

70 Seiler, S. *et al.* The phosphatonin fibroblast growth factor 23 links calcium-phosphate metabolism with left-ventricular dysfunction and atrial fibrillation. *Eur Heart J* 32, 2688-2696, doi:10.1093/eurheartj/ehr215 (2011).

71 Andersen, I. A., Huntley, B. K., Sandberg, S. S., Heublein, D. M. & Burnett, J. C., Jr. Elevation of circulating but not myocardial FGF23 in human acute decompensated heart failure. *Nephrol Dial Transplant* 31, 767-772, doi:10.1093/ndt/gfv398 (2016).

72 Andrukhova, O., Slavic, S., Odorfer, K. I. & Erben, R. G. Experimental Myocardial Infarction Upregulates Circulating Fibroblast Growth Factor-23. *J Bone Miner Res* 30, 1831-1839, doi:10.1002/jbmr.2527 (2015).

73 Touchberry, C. D. *et al.* FGF23 is a novel regulator of intracellular calcium and cardiac contractility in addition to cardiac hypertrophy. *Am J Physiol Endocrinol Metab* 304, E863-873, doi:10.1152/ajpendo.00596.2012 (2013).

74 Navarro-Garcia, J. A. *et al.* Fibroblast growth factor-23 promotes rhythm alterations and contractile dysfunction in adult ventricular cardiomyocytes. *Nephrol Dial Transplant* 34, 1864-1875, doi:10.1093/ndt/gfy392 (2019).

75 Huang, S. Y. *et al.* Fibroblast growth factor 23 dysregulates late sodium current and calcium homeostasis with enhanced arrhythmogenesis in pulmonary vein cardiomyocytes. *Oncotarget* 7, 69231-69242, doi:10.18632/oncotarget.12470 (2016).

76 Kao, Y. H. *et al.* FGF-23 dysregulates calcium homeostasis and electrophysiological properties in HL-1 atrial cells. *Eur J Clin Invest* 44, 795-801, doi:10.1111/eci.12296 (2014).

77 Xie, J. *et al.* Cardioprotection by Klotho through downregulation of TRPC6 channels in the mouse heart. *Nat Commun* 3, 1238, doi:10.1038/ncomms2240 (2012).

78 Olejnik, A., Krzywonos-Zawadzka, A., Banaszkiewicz, M. & Bil-Lula, I. Klotho protein contributes to cardioprotection during ischaemia/reperfusion injury. *J Cell Mol Med* 24, 6448-6458, doi:10.1111/jcmm.15293 (2020).

79 Hu, M. C. *et al.* Recombinant alpha-Klotho may be prophylactic and therapeutic for acute to chronic kidney disease progression and uremic cardiomyopathy. *Kidney Int* 91, 1104-1114, doi:10.1016/j.kint.2016.10.034 (2017).

80 Hung, Y. *et al.* Klotho modulates electrical activity and calcium homeostasis in pulmonary vein cardiomyocytes via PI3K/Akt signalling. *Europace* 22, 1132-1141, doi:10.1093/europace/euaa100 (2020).

81 Mizia-Stec, K. *et al.* Lower soluble Klotho and higher fibroblast growth factor 23 serum levels are associated with episodes of atrial fibrillation. *Cytokine* 111, 106-111, doi:10.1016/j.cyto.2018.08.005 (2018).

82 Baruscotti, M., Barbuti, A. & Bucchi, A. The cardiac pacemaker current. *J Mol Cell Cardiol* 48, 55-64, doi:10.1016/j.yjmcc.2009.06.019 (2010).

83 Smith, E. R., Cai, M. M., McMahon, L. P. & Holt, S. G. Biological variability of plasma intact and C-terminal FGF23 measurements. *J Clin Endocrinol Metab* 97, 3357-3365, doi:10.1210/jc.2012-1811 (2012).

84 Lu, Z. *et al.* Regulation of HCN2 Current by PI3K/Akt Signaling. *Front Physiol* 11, 587040, doi:10.3389/fphys.2020.587040 (2020).

85 Lin, R. Z. *et al.* Regulation of heart rate and the pacemaker current by phosphoinositide 3-kinase signaling. *J Gen Physiol* 151, 1051-1058, doi:10.1085/jgp.201812293 (2019).

86 Yang, M. *et al.* Adiposederived stem cells overexpressing SK4 calciumactivated potassium channel generate biological pacemakers. *Int J Mol Med* 44, 2103-2112, doi:10.3892/ijmm.2019.4374 (2019).

87 Aziz, Q., Li, Y. & Tinker, A. Potassium channels in the sinoatrial node and their role in heart rate control. *Channels (Austin)* 12, 356-366, doi:10.1080/19336950.2018.1532255 (2018).

88 Andrukhova, O. *et al.* FGF23 acts directly on renal proximal tubules to induce phosphaturia through activation of the ERK1/2-SGK1 signaling pathway. *Bone* 51, 621-628, doi:10.1016/j.bone.2012.05.015 (2012).

89 Viggiano, D. & Pollastro, R. M. Relation among Blood Pressure, Heart Rate and Creatinine in Kidney Transplanted Patients. *Insights in Blood Pressure* 1, doi:ISSN 2471-9897 (2015).

90 Baruscotti, M. *et al.* Deep bradycardia and heart block caused by inducible cardiac-specific knockout of the pacemaker channel gene Hcn4. *Proc Natl Acad Sci U S A* 108, 1705-1710, doi:10.1073/pnas.1010122108 (2011).

91 Benzoni, P. *et al.* Human iPSC modelling of a familial form of atrial fibrillation reveals a gain of function of If and ICaL in patient-derived cardiomyocytes. *Cardiovasc Res* 116, 1147-1160, doi:10.1093/cvr/cvz217 (2020).

92 Tate, C. M. *et al.* A BMP7 Variant Inhibits Tumor Angiogenesis In Vitro and In Vivo through Direct Modulation of Endothelial Cell Biology. *PLoS One* 10, e0125697, doi:10.1371/journal.pone.0125697 (2015).

93 Yang, J. *et al.* Binding of FGF2 to FGFR2 in an autocrine mode in trophectoderm cells is indispensable for mouse blastocyst formation through PKC-p38 pathway. *Cell Cycle* 14, 3318-3330, doi:10.1080/15384101.2015.1087622 (2015).

The three Greek Goddesses. **Clotho** is the one who spins the thread of human life, Lachesis measures its length and Atropos cuts it.